



Output-Only Method for Defect Identification in the Internal Edge of the Plates with a Circular Hole Using Guided Ultrasonic Waves and Discrete Wavelet Transform

Mohammadreza Jalalinia¹ · Gholamreza Ghodrati Amiri¹ · Seyed Ali Seyed Razzaghi²

Received: 24 May 2021 / Accepted: 12 January 2022 / Published online: 12 March 2022
© Shiraz University 2022

Abstract

This article proposed a baseline-free method for damage localization in plates with a circular hole. Damages are defined as cracks at the internal edge of the hole with different lengths and angles. Guided ultrasonic waves (GUWs) are used to excite the plate and receive feedback with a pitch-catch active sensing configuration. The numerical simulations conducted in ABAQUS and GUWs are generated by simulating circular piezoelectric transducers located at the top surface of the plate. In this study, transducers are located on the plate in such a way that similar paths are made for waves traveling from actuators to sensors. In these similar paths, the sensor spacing of transmitter–receiver paths should be equal. Then, the first wave packet of response signals acquired by sensors is processed by discrete wavelet transform to extract actionable damage-sensitive features. The features obtained for similar paths are compared to calculate damage indexes which are used to locate damage. The numerical results reveal that the proposed method can precisely identify the location of cracks in a holed plate, only by measuring the wavelet energy of approximate coefficients at the first and second levels of wavelet decomposition. For paths in a group of similar paths, the material and geometrical properties of the structure, the actuator–sensor distance between similar paths and the sensitivity of the probing devices must be the same. In the process of sensor installation, the lengths of the paths in a group may not be equal to each other. In this paper, the effects of small differences between the measurement paths, which are supposed to be essentially the same, on the accuracy of damage detection results are investigated.

Keywords Non-destructive evaluation · Baseline-free · Discrete wavelet transform · Guided ultrasonic waves · Crack detection · Plate with hole

1 Introduction

Member-wise nondestructive testing (NDT) and evaluation have captured considerable attention in industrial applications regarding defect localization and identification (Cawley 2018; Liu et al. 2020). Several nondestructive evaluation methods were designed, given various needs of industries. Guided ultrasonic waves (GUWs) are particularly suitable for precise and fast damage detection applications because

of propagation at long distances with little amplitude loss (Bourasseau et al. 2000). Lamb waves are the most commonly used GUWs in defect detection using pulse-echo (Alleyne et al. 2004), pitch-catch (Ihn and Chang 2008), and time-reversal (Sohn et al. 2007) techniques. GUWs have been successfully applied in plates (Ghadami et al. 2018; Ebrahimkhanlou and Salamone 2018), beams, and rods (Kim et al. 2019) for damage detection. Many researchers use GUWs propagation and compare collected waves from the intact and damaged structures as the most common approaches to detect damage in different structural systems (Zhou et al. 2013). The aim of nondestructive evaluation is to detect and extract damage-sensitive features capable of providing data for determining the existence, location, and severity of the defect (Bagheri et al. 2013; Rubio et al. 2019). Among various algorithms, time of flight and amplitude change are the most commonly used damage indexes for damage identification. Most amplitude change-based

✉ Gholamreza Ghodrati Amiri
ghodrati@iust.ac.ir

¹ Natural Disasters Prevention Research Center, School of Civil Engineering, Iran University of Science and Technology, P.O. Box 16765-163, Narmak, Tehran, Iran

² Department of Civil Engineering, Payame Noor University, Tehran, Iran

methods rely on collecting reference signals in undamaged conditions (Lee and Staszewski 2007; Hua et al. 2020). In addition, conventional time of flight-based algorithms are not appropriate under circumstance where there is more than one instance of damage due to dispersion phenomena and multi-modal nature of Lamb wave propagation in the structures. In this case, much more complex and multi-faceted scattered Lamb wave components (from multiple damage and structural boundaries) are captured, where the signatures of different instances of damage significantly overlap with each other (Wang et al. 2009). As a result, it is extremely time-consuming and sometimes impractical to isolate them individually. In the conventional structural health monitoring (SHM) techniques using GUWs, signal processing methods are adopted for reducing the complexity of the received Lamb wave signals. Various methods such as fast Fourier transform, short time Fourier transform, wavelet transform, and Hilbert–Huang transform were developed for processing the received signal. Fast Fourier transform is a frequency domain analysis used to extract frequency domain features. In the frequency domain analysis, we lose the time information such as arrival time and dispersion. In recent years, discrete wavelet transform-based (DWT) (Lanza Discalea et al. 2007; Rizzo and di Scalea 2006) and continuous wavelet transform-based (CWT) methods (Grabowska et al. 2008; Giridhara et al. 2010) have been employed to detect the dispersive guided wave signal features. DWT- and CWT-based methods effectively de-noise, compress, and characterize the time–frequency content of nonstationary signals. Bagheri et al. (2013) presented a reference-free approach for SHM of plate-like structures using GUWs and signal processing. The reference-free approach includes the extraction of damage-sensitive features from the signals processed utilizing the CWT and the empirical mode decomposition (EMD) combined with the Hilbert spectrum analysis. When random noise was added to the numerical signals, the damage indexes obtained from the wavelet-based feature detected the damage more accurately than those obtained from the EMD-based feature. Alem et al. (2016) compared two instantaneous baseline damage detection techniques based on cross-correlation (CC) analysis and wavelet analysis. For a damaged plate, the damage index values obtained from the wavelet analysis are greater than those obtained from the CC algorithm. Given that actual monitoring systems always contain noise, which may affect the performance of an algorithm, the wavelet-based method is more potent in diagnosing the damage than the correlation-based method. Small damage index values make it challenging to recognize the damaged path.

Local monitoring is a type of SHM techniques that monitors a small area immediately adjacent to the sensor (Yu et al. 2010). They can be used to monitor the progress of damage already identified in routine NDT or monitoring the

known hot-spots (Cawley 2018). Local monitoring can be conducted in areas with high-stress concentrations with a high probability of cracking. The existence of some holes in a plate disturbs the continuum of material. Thus, when an external load (such as uniform tension) is applied to this plate, stress concentration arises in the proximity of the holes; as a result, the cracks can appear. Failure to detect the cracks at the hole edge can grow them until destroying the whole structure. Recently, many researchers are focused only on detection of the crack at the hole edge with the use of guided wave propagation method. Liu et al. (2013) presented an approach for crack detection problems in a rivet joint using lamb wave, CWT, and neural networks. The wavelet transform is used to extract a robust and effective feature called energy ratio change from time domain signals. To calculate this feature, the energy ratio calculated by the CWT should be compared to the energy ratio of an intact sample. One neural network is first used to diagnose plate integrity. If cracks are detected, then the second neural network is called to determine their locations. Wang et al. (2017) presented a nonlinear Lamb-wave-based method for fatigue crack detection in steel plate and carbon fiber reinforced polymer (CFRP) steel plate with a through-thickness hole and initial notches in the middle. With the generation of the second harmonic, the damage-induced wave nonlinearities are identified by surface-bonded piezoelectric sensors. Chiu et al. (2017) presented a computational study of the interaction between the edge-guided wave and small crack on a circular hole in an aluminum plate. It is shown that edge waves traveling on the curved surface leak energy into the medium, unlike those travelling on a straight surface which do not attenuate, and the scattered field generated by their interaction with an edge crack is investigated. Schubert Kabban et al. (2018) proposed a simulation model to determine the SHM sensitive factors to enable SHM validation. For this purpose, the guided Lamb waves traveling through an aluminum plate were used to detect the damage caused by the growth of butterfly cracks from a rivet hole. Dai et al. (2019) used a PZT-based active sensing method with an improved sensor design to detect the porous aluminum alloy plate hole-edge corrosion. The mentioned studies are mainly concerned with small holes in rivet joints. Stawiarski et al. (2017) used the elastic wave propagation phenomenon to detect the fatigue crack initiation in the isotropic plate with a relatively large circular hole. This hole is located in the geometrical center of a rectangular plate made of aluminum alloy. Barski and Stawiarski (2018) also proposed two different system variants for detecting and evaluating crack length in the case of relatively large holes. The system, which demands the reference information obtained for an intact structure, provides a better estimation of the actual size of the damage. However, in the SHM system, which works without the signal from the intact structure,

the maximal length of a crack is about 24 mm, which can be monitored. In this work, the most dangerous point must first be predicted at the hole edge where the damage may be initialized, and the sensors placed exactly around the crack. In some structures, it is complicated to predict such points. The currently presented work is devoted to the problem of detecting the location of cracks at the edge of relatively large circular holes. The crack may have grown along the hole radius or with an angle. In this work, the location of the crack created at the edge of the hole is not predictable.

Generally, most SHM methods rely on the comparison of defected and intact structure for any defects. It is usually difficult or even impossible to have access to the baseline data. In this article, a baseline-free approach was adopted to identify the crack location at the edge of the circular hole. This approach utilizes pitch-catch data for damage detection. A finite element model in ABAQUS is employed to simulate the propagation of elastic guided waves in damaged plate-like structure containing a circle hole. At first, Lamb waves are generated applying a four-cycle sinusoidal tone burst electrical potential function on simulated piezoelectric transducer (PZT) actuators. These PZTs are considered on a circle concentric with hole. According to sensor spacing, all sensor–actuator paths are divided into some groups, each having similar paths. Damaged paths are identified for each group of similar paths by comparing energies product of approximate coefficients obtained from the DWT of the first symmetric mode of the output signal in different levels. Then, the damage is localized at the hole edge by measuring this energy for all the sensing paths and applying a probabilistic approach. Furthermore, the method sensitivity to uncertainty in the distance of similar paths is numerically investigated using a finite element method (FEM).

2 Wavelet-Based Signal Processing

Wavelet transform (WT) eliminates noise and computes a damage index from the recorded Lamb wave ultrasonic signals (Legendre et al. 2000; Xu et al. 2021; Gómez Muñoz et al. 2019; Bagheri et al. 2017). Wavelet functions are a mixture of basic functions that separate time and frequency domain signals. WT presents some advantages improving the limitations of resolution and the loss of information presented by the short-time Fourier transform or the fast Fourier transform. The main feature of the WT is using a variable window size, which adjusts it to the frequency according to the information in the high or low-frequency signal (Mallat 1989). Through the flexible window, WT can perform multi-resolution analysis so that shorter windows are used for analyzing high frequencies of a signal and broader windows for analyzing low frequencies of a signal (Stark 2005). This capability is given by the mother wavelet function ψ , defined

by scaling parameter a , and shifting (translation) parameter b . The wavelet function at scale (dilation or contraction) a , and location b is as (Addison 2002):

$$\psi_{a,b}(t) = \frac{1}{\sqrt{a}} \psi\left(\frac{t-b}{a}\right) \quad (1)$$

Nonetheless, there are two main trends in the application of WTs, using either CWT or the DWT. The CWT of a signal $x(t)$ is defined as the integral of the signal multiplied by scaled and shifted versions of a wavelet function ψ and is given by Eq. (2) (Addison 2002):

$$\text{CWT}(a, b) = \int_{-\infty}^{+\infty} x(t) \frac{1}{\sqrt{a}} \psi\left(\frac{t-b}{a}\right) dt \quad (2)$$

Calculation of wavelet coefficients at every possible scale could lead to a redundant result which may not always be desirable. To overcome the redundancy problem, mother wavelet discretization for discrete steps in scales and translations is done through DWT. Such a discrete wavelet has the form (Addison 2002):

$$\psi_{m,n}(t) = a_0^{-m/2} \psi(a_0^{-m}t - nb_0) \quad (3)$$

where the integers m and n control the wavelet dilation and translation, respectively. Also, a_0 is a specified fixed dilation step parameter at a value greater than 1, and b_0 is the location parameter which should be greater than 0. The common selection for the discrete parameters a_0 and b_0 is 2 and 1, respectively. This logarithmic scaling is known as dyadic array. The dyadic grid wavelet is expressed

$$\psi_{m,n} = 2^{-m/2} \psi(2^{-m}t - n) \quad (4)$$

The DWT of the guided wave signal $S(t)$ is defined as:

$$T_{m,n} = \frac{1}{\sqrt{2^m}} \int_{-\infty}^{+\infty} S(t) \psi(2^{-m}t - n) dt \quad (5)$$

where $T_{m,n}$ are the wavelet coefficients related to the wavelet function $\psi_{m,n}$ at the resolution level m and each of the elements in the time series n . Multi-resolution analysis (MRA) is the fundamental approach of DWT, introduced by Mallat (1989). In the first step of the DWT, a signal S is segregated into an approximation $A^{(1)}$ and detail $D^{(1)}$ by passing the signal through a series of low-pass g and high-pass h filter pairs. According to the Nyquist rule, the output signals having half the frequency bandwidth of the original signals can be down-sampled by two (Kumar et al. 2012). The approximation coefficients can provide information about low frequencies components of the signal, and detail coefficients can obtain information about high-frequency components.

The same procedure can be performed on approximation coefficients $A^{(1)}$ in order to obtain decomposition in finer scales: ($A^{(1)} = A^{(2)} + D^{(2)}$). At each stage of the decomposition process, the resolution of frequency is doubled through filtering. The decomposition of a signal S to different scales of resolution m is obtained by applying the DWT to S . The decomposition process is shown schematically in Fig. 1.

The decomposition of discrete approximation $A_l^{(m-1)}$ into two components detail coefficients $D_n^{(m)}$ (from the high-pass filter h) and approximation coefficients $A_n^{(m)}$ (from the low-pass filter g) can be calculated using the following relations:

$$\begin{aligned}
 A_n^{(m)} &= \sum_l g_{2n-l} A_l^{(m-1)} \\
 D_n^{(m)} &= \sum_l h_{2n-l} A_l^{(m-1)}
 \end{aligned}
 \tag{6}$$

where m is the level of decomposition and n is each element in the time series. Assume f_s as the guided wave signal $S(t)$ sampling frequency. Following the Nyquist criterion, the maximum useful frequency that should be applied is half of the sampling frequency (Kumar et al. 2012). Therefore, the frequency band decomposed by DWT is $[0, f_s/2]$. In the first level decomposition, the signal S is simultaneously passed through a low-pass g and high-pass h filter. According to wavelet analysis theory, the $A^{(1)}$ and $D^{(1)}$ wavelet coefficients have a frequency band of $[0, f_s/4]$ and $[f_s/4, f_s/2]$, respectively. In the second level of decomposition, the $A^{(1)}$ coefficient obtained from the first level is decomposed to $A^{(2)}$ and $D^{(2)}$ wavelet coefficient sets that correspond to $[0, f_s/8]$ and $[f_s/8, f_s/4]$, respectively. Generally, the approximation coefficients $A^{(m)}$ and the detail coefficients $D^{(m)}$ have half the frequency bandwidth of the approximation coefficients $A^{(m-1)}$ at each decomposition level m . The frequency bands of the information contained in detail $D^{(m-1)}$ and approximation $A^{(m-1)}$ for each decomposition level m are obtained as follows:

$$\begin{aligned}
 D^m(n) &: [2^{-(m+1)}f_s, 2^{-m}f_s] \\
 A^m(n) &: [0, 2^{-(m+1)}f_s]
 \end{aligned}
 \tag{7}$$

where $[,]$ represents the frequency band, f_s is the sampling frequency of the signal S , and n is each element in the time series.

In real monitoring systems, the Lamb wave signals recorded by sensors are often polluted by noise which directly affect their accuracy of measurement. In this research, unnecessary

information such as noise in the measured signals is discarded using DWT. Then, the location of the damage is identified using the energy of the obtained approximation coefficients A^m . It should be noted that more decompositions levels do not always mean better accurate results. As the number of decomposition levels increases, some of the damage information contained in the received signals may be removed. Here, the B-spline mother wavelet of order 4 as shown in Fig. 2 is used to analyze guided waves signal due to its similarity to excitation shape. In section "Damage identification in the plate with a circular hole," the features extracted from the DWT of wave signals to identify damage are described.

3 Finite Element Simulation

In this research, a 600 mm × 600 mm × 1.59 mm cantilever aluminum plate containing a circular hole with a radius of 40 mm was considered. The characteristics of the homogenous, linear elastic, and isotropic material of the aluminum plate (Al-6061) were as follows: density $\rho = 2700 \text{ kg/m}^3$, Young modulus $E = 68.9 \text{ GPa}$ and Poisson's ratio $\nu = 0.33$. Four case studies are considered in this paper. In the first, the center of the hole is located at the center of the plate ($x_h = 300, y_h = 300$) mm. In the second, third, and fourth case studies, the center of the hole is located at (150, 300) mm, (140, 300) mm, and (130, 300) mm, respectively (see Fig. 3). The origin of coordinates is located at the lower left

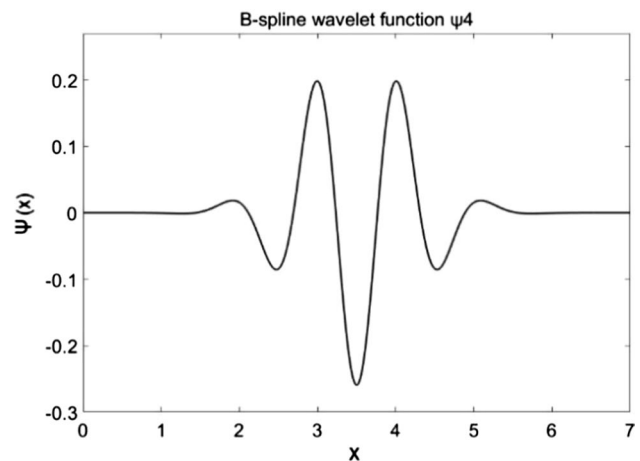
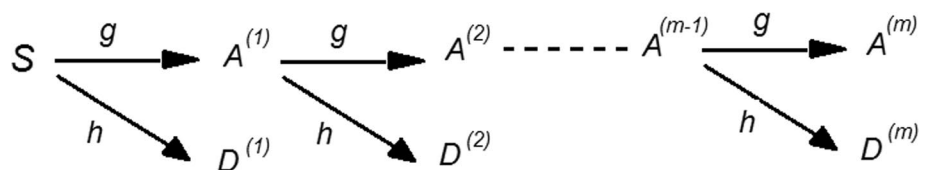


Fig. 2 One-dimensional fourth-order B-spline wavelet function ψ_4

Fig. 1 Schematic illustration of the DWT implementation using a filter bank structure



corner of the plate. In this study, four damage cases were considered on the hole. In the first, second, and third damage cases, the crack was considered along with the radius of the hole with dimensions 5 mm × 1 mm × 1.59 mm, 10 mm × 1 mm × 1.59 mm, and 25 mm × 1 mm × 1.59 mm at the edge of the hole, respectively. In the fourth damage case, an inclined crack was considered at 45° with respect to the radial crack regarded in the third case, respectively. Figures 3 and 4 show the geometry of the plate and the damage location, respectively.

To detect the defect in this plate, “ $N=12, 18, \text{ and } 24$ ” circular piezoelectric transducers with a diameter 12.7 mm and 0.254 mm in thickness situated on the surface were regarded (N is the number of transducers). In the first case study (in which the hole is in the plate center), these transducers were placed on a circle concentric with hole, and the radius r ($r=110, 165 \text{ or } 220 \text{ mm}$). In the other three

case studies, the transducers were placed only on a 110 mm radius circle circumference due to the hole proximity to the plate boundary. It simulates the presence of a circular array of transducers bonded into aluminum plate. Figure 5 shows PZTs configuration in the aluminum plate with damage for ($N=24 \text{ and } r=165 \text{ mm}$).

The material properties of PZT used in FE simulation are listed in Table 1. (Note that $\epsilon_0=8.85 \times 10^{-12} \text{ F/m}$ is the permittivity of free space.)

A wave always takes minimum energy path to travel between any two points in the plate. For a homogeneous isotropic medium, this minimum path is the shortest distance (Masurkar and Yelve 2017). If the straight line between the actuator and sensor does not pass through the hole, the first wave packet travels along the line of sight between the actuator and the sensor. In this paper, the transmitted wave from each of the PZT actuators is measured by three other PZT sensors. The three PZT sensors are selected so that the straight line between the actuator and the sensor does not

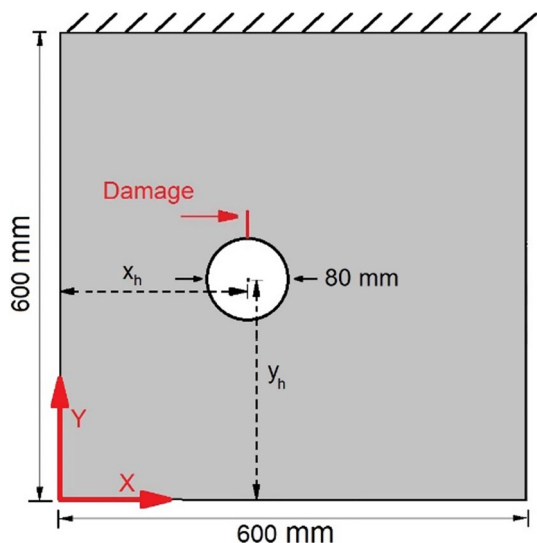


Fig. 3 Geometry of the damaged plate with a circular hole

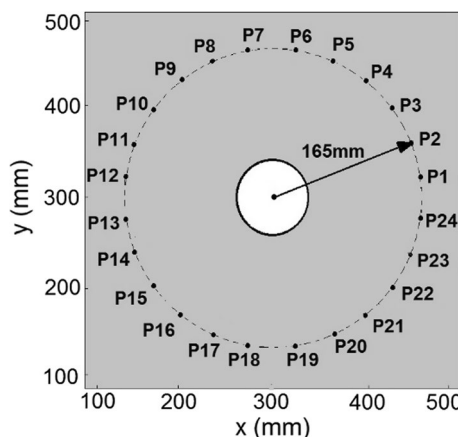


Fig. 5 Configuration of the multipoint measuring system with a damage for $N=24$ and $r=165 \text{ mm}$

Fig. 4 Location of damage for a crack case 1–3, b crack case 4

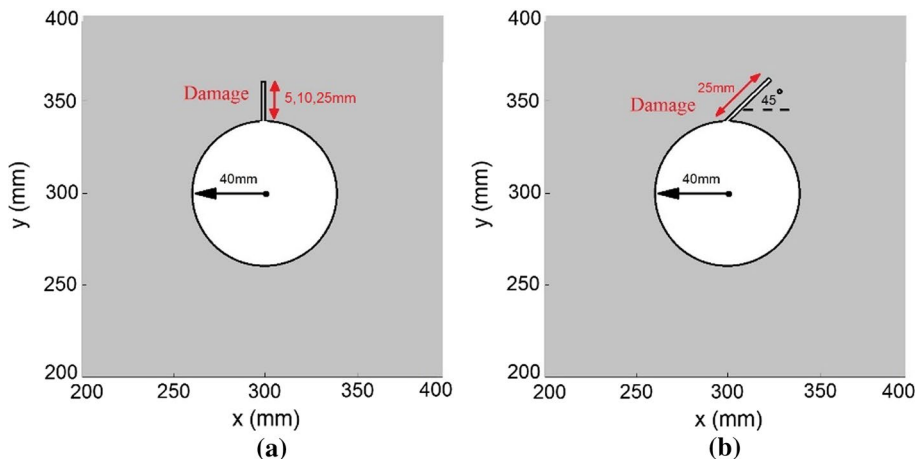


Table 1 Properties of simulated PZT

Property	Symbol (Unit)	value
Density	ρ (kg/m ³)	7700
Young's modulus (in the plane direction)	E_1, E_2 (GPa)	63
Young's modulus (in the out-of-plane direction)	E_3 (GPa)	54
Poisson's ratio	$\nu_{12}, \nu_{13}, \nu_{23}$	0.35
Piezoelectric coefficient	d_{31} (m/V)	-175×10^{-12}
	d_{32} (m/V)	-175×10^{-12}
	d_{33} (m/V)	400×10^{-12}
	d_{15} (m/V)	590×10^{-12}
	d_{24} (m/V)	590×10^{-12}
Relative dielectric constant	$\epsilon_{33}^T/\epsilon_0$	1900

pass through the hole. Because for these paths, the traveling path of the first wave packet is easily recognizable. In addition, only the signals whose sight line of the actuator–sensor passes near the hole edge are measured to detect cracks created at the edge of the hole. For example, in the case of 24 transducers ($N=24$) at distance of 165 mm ($r=165$ mm), when an excitation wave is sent from one of the PZT actuators situated around the hole ($P_i, i=1, 2, \dots, 24$), the electric potential output of the following sensors is monitored and collected.

$$\begin{cases} \text{for } i = 1, 2, \dots, 14 & \Rightarrow P_{i+8}, P_{i+9}, P_{i+10} \\ \text{for } i = 15 & \Rightarrow P_1, P_{23}, P_{24} \\ \text{for } i = 16 & \Rightarrow P_1, P_2, P_{24} \\ \text{for } i = 17, 18, \dots, 24 & \Rightarrow P_{i-16}, P_{i-15}, P_{i-14} \end{cases} \quad (8)$$

After applying the excitation wave in each of the transducers (P_1, P_2, \dots, P_{24}), the signals of the three transducers mentioned in relation 8 were measured. For example, for $i=1$, when an excitation wave is applied to the transducer P_1 , the signals of the three transducers P_9, P_{10} and P_{11} are measured. Given the number and location of the transducers, a sum of $24 \times 3 = 72$ sensing paths was made. In all these paths, the distances between each actuator and the three sensors were 318.8 mm, 304.9 mm, and 285.8 mm. These sensing paths were divided into three groups of similar paths.

The paths mentioned in each group have an equal path length and the same position to the edges of the hole. For $N=24$ and $r=165$ mm, this grouping is shown in Table 2. Figure 6a–c shows all considered paths with three different path lengths schematically.

The number and location of the transducers as well as selected paths and grouping were considered in a way that all areas around the circular hole of the plate were examined for damages. As shown in Fig. 6a, the connecting line of each actuator–sensor pair mentioned in group 1 passes near the edge of the hole. Therefore, if a crack is occurs at the hole edge, its initial part is in the straight line between the sensor and actuator of some of the paths mentioned in this group. By increasing the length of the crack created at the edge of the hole, a part of the crack is placed in a straight line between the actuator and sensor of the paths mentioned in groups 2 and 3 (see Fig. 6b, c). In this paper, only three groups of similar paths are considered and other signals of similar paths with shorter lengths (e.g., P_1 – P_8, P_1 – P_7 and P_2 – P_9) are ignored. This is because only the end part of a large crack passes through or near the sensor–actuator straight line of these similar short paths. The long cracks can be identified by eye inspection.

In other cases, three groups of similar paths have been defined similarly to the mentioned method for $N=24$ and $r=165$ mm. Figure 7a–c shows an example of the three

Table 2 Grouping all of the sensing paths and the geometric distance

Group	Sensing path	Actuator–sensor distance (mm)
1	P_1 – P_{11}, P_2 – P_{12}, P_3 – P_{13}, P_4 – P_{14}, P_5 – P_{15}, P_6 – P_{16}, P_7 – P_{17}, P_8 – P_{18}, P_9 – P_{19}, P_{10} – P_{20}, P_{11} – P_{21}, P_{12} – P_{22}, P_{13} – P_{23}, P_{14} – P_{24}, P_{15} – P_1, P_{16} – P_2, P_{17} – P_3, P_{18} – P_4, P_{19} – P_5, P_{20} – P_6, P_{21} – P_7, P_{22} – P_8, P_{23} – P_9, P_{24} – P_{10}	318.8
2	P_1 – P_{10}, P_2 – P_{11}, P_3 – P_{12}, P_4 – P_{13}, P_5 – P_{14}, P_6 – P_{15}, P_7 – P_{16}, P_8 – P_{17}, P_9 – P_{18}, P_{10} – P_{19}, P_{11} – P_{20}, P_{12} – P_{21}, P_{13} – P_{22}, P_{14} – P_{23}, P_{15} – P_{24}, P_{16} – P_1, P_{17} – P_2, P_{18} – P_3, P_{19} – P_4, P_{20} – P_5, P_{21} – P_6, P_{22} – P_7, P_{23} – P_8, P_{24} – P_9	304.9
3	P_1 – P_9, P_2 – P_{10}, P_3 – P_{11}, P_4 – P_{12}, P_5 – P_{13}, P_6 – P_{14}, P_7 – P_{15}, P_8 – P_{16}, P_9 – P_{17}, P_{10} – P_{18}, P_{11} – P_{19}, P_{12} – P_{20}, P_{13} – P_{21}, P_{14} – P_{22}, P_{15} – P_{23}, P_{16} – P_{24}, P_{17} – P_1, P_{18} – P_2, P_{19} – P_3, P_{20} – P_4, P_{21} – P_5, P_{22} – P_6, P_{23} – P_7, P_{24} – P_8	285.8

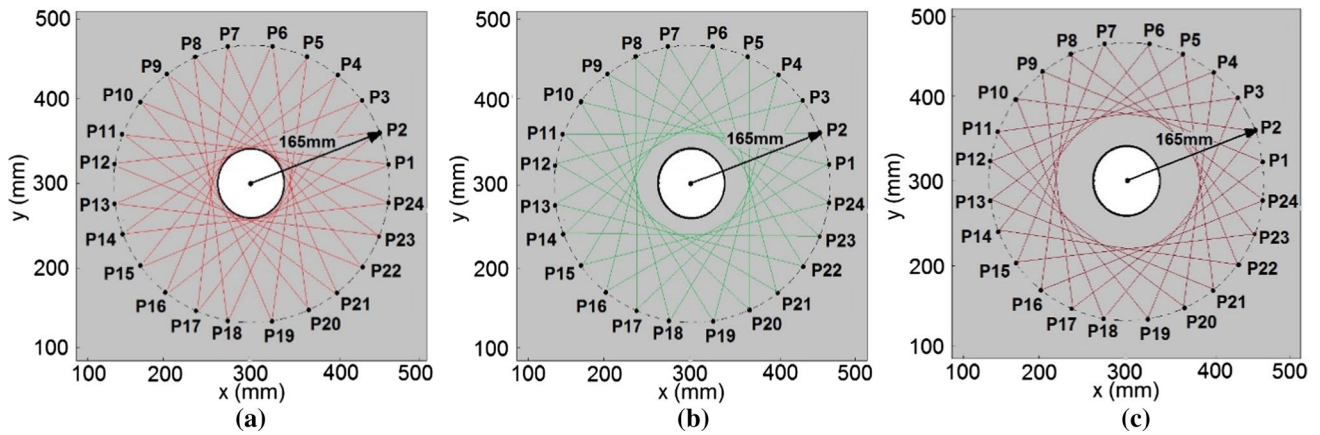


Fig. 6 Schema of the multipoint measuring system with three different path lengths for $N=24$ and $r=165$ mm; a 318.8 mm, b 304.9 mm, c 285.8 mm

considered paths for $N=12, 18,$ and $24,$ respectively. In this figure, the simulated PZTs are placed at distances $r=110$ mm, $r=165$ mm and $r=220$ mm.

In this paper, the propagation of guided waves in the structures was numerically simulated by the standard commercial software Abaqus v.6.14-5. The propagation of Lamb waves in plate-like structures is accurately simulated in Abaqus using the dynamic explicit time-step analysis (Alem et al. 2016). However, multi-physics or fully coupled PZT elements can only be used in the time integration implicit solver in the Abaqus elements library. Therefore, implicit- and explicit-dynamic analyses should be coupled to achieve acceptable results. An Abaqus co-simulation model can allow different solvers to calculate in piezoelectric transducer and the host structure (Wang 2014). Therefore, a standard–explicit co-simulation interface is considered for the lower surface of PZTs to link its elements to aluminum

plate elements. The aluminum plate was meshed with eight-node standard solid element C3D8R with three degrees of freedom per node and simulated under Abaqus/Explicit code. Also, PZTs were meshed with an eight-node linear piezoelectric brick element C3D8E and simulated under Abaqus/Implicit code. In this method, the output of piezoelectric analysis was used as an input of transient dynamic analysis in the explicit analysis. In each time increment, the data were exchanged between two solvers through an interactive interface between the PZT actuator and aluminum plate in a synchronized manner.

The excitation signal frequency is an important parameter which should be correctly chosen to achieve more reliable damage detection results. Excitation signal frequency should be low enough, where only the first symmetric mode S_0 and the first anti-symmetric mode A_0 are propagated in the structure. Dispersion curves of phase

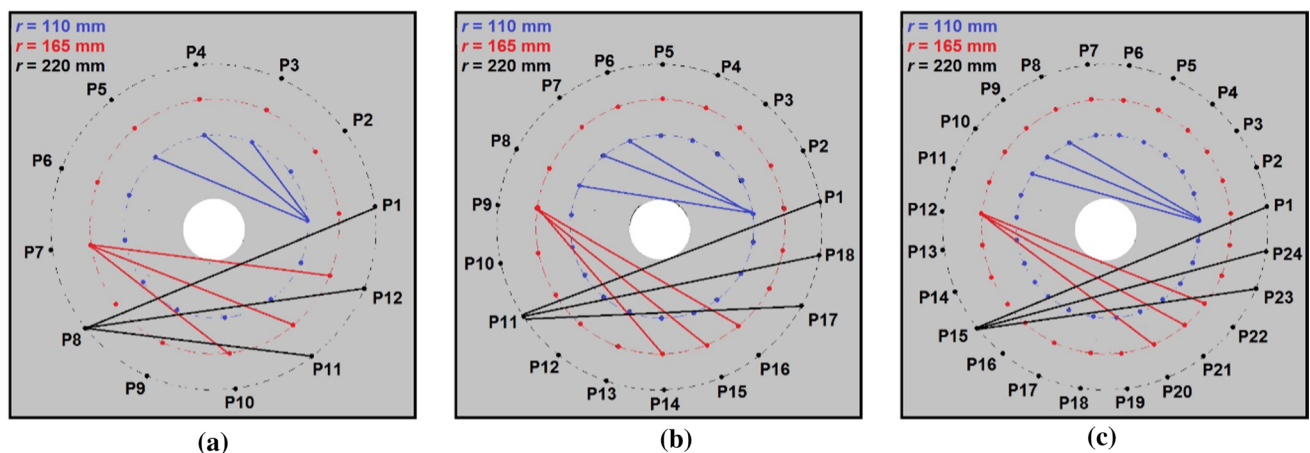


Fig. 7 Schema of the multipoint measuring system with three different path lengths for a $N=12,$ b $N=18,$ c $N=24,$ when the simulated PZTs are placed at distances $r=110$ mm, $r=165$ mm or $r=220$ mm

velocities for 1.59-mm-thick 6061 aluminum plate are presented in Fig. 8a. It can be seen that central frequency of the generated wave should be less than 1 MHz. This study generated Lamb waves by applying a four-cycle sinusoidal tone burst electrical potential function with a 200-kHz center frequency and a peak-to-peak amplitude of 10 V to the PZT actuator (Fig. 8b).

In dynamic time-step analysis, the precision of the procedure depends on the temporal and spatial resolution of the analysis. In general, the computational accuracy of the model can be improved with an increasingly smaller integration time step. A small time step increases the computation load; meanwhile, a large time step cannot resolve high frequency components. Therefore, an appropriate integration time step should be chosen. In this paper, the choice of time step (Δt) follows two criteria in Eqs. (9) and (11). Equation (9) is the Courant–Friedrichs–Lewy (CFL) condition, which dictates that the fastest propagating wave, i.e., the bulk longitudinal wave c_L , should not travel more than one element in a single time step (Courant et al. 1967; Ng and Veidt 2009; He et al. 2017). The time step calculation can be expressed as:

$$\Delta t \leq \frac{L_{\min}}{c_L} \tag{9}$$

where L_{\min} is the smallest dimension of the smallest finite element of the model. The longitudinal wave speed (c_L) can be calculated from the following equation (He et al. 2017):

$$c_L = \sqrt{\frac{E(1-\nu)}{\rho(1-2\nu)(1+\nu)}} = \sqrt{\frac{68.9 \times 10^9 \times (0.67)}{2700 \times 0.34 \times 1.33}} = 6148.93 \text{ m/s} \tag{10}$$

However, Jingpin et al. (2017) recommended $\Delta t < 0.7L_{\min}/c_L$. Another criterion for time step resolution Δt is to use a minimum of 20 points per cycle at the highest frequency f_{\max} (Moser et al. 1999; Bartoli et al. 2005; Wan et al. 2014; Gresil et al. 2012) so that:

$$\Delta t \leq \frac{1}{20f_{\max}} = \frac{1}{20 \times 200000} = 0.25 \mu\text{s} \tag{11}$$

The lowest phase velocity, and hence the shortest wavelength, sets the maximum permissible grid spacing that must be chosen so that spatial aliasing due to the finite element discretization does not occur (Faccioli et al. 1997). The element size is chosen in a manner so that the propagation waves can spatially be resolved. For this purpose, usually more than 10 nodes in wavelength are required (Moser et al. 1999; Bartoli et al. 2005). This condition can be written as

$$L_e \leq \frac{\lambda_{\min}}{10} \tag{12}$$

where L_e is the element size and λ_{\min} is the wavelength corresponding to the highest frequency of the propagated wave mode. For the frequency of 200 kHz, the minimum wavelength is for A_0 , which is given by $\lambda_{\min} = c/f_{\max} = 7.9 \text{ mm}$, considering a theoretical phase velocity of $c = 1.58 \text{ km/s}$ (Bartoli et al. 2005). Accordingly, the element size of 0.79 mm is used for the simulation. The CFL condition relates the mesh size and the time step in the numerical model as mentioned in Eq. (9) (Courant et al. 1967; Faccioli et al. 1997; He et al. 2017). Based on the CFL condition, the stable time step chosen should be less than 0.128 μs . Therefore, the maximum time step is set to be 0.11 μs based on Eqs. (9) and (11).

The Von Mises stress contour graphs are shown in Fig. 9a, b at 33 μs and 48 μs , respectively, when the 4-cycle tone burst is applied to the transducer P2. In time 33 μs , the first wave packet (S_0 mode) arrives at the damage, and in time 48 μs , this wave passes through the defect partly reflected by the defect.

Figure 10 shows the symmetric part of numerical output wave resulting from the similar sensing paths P1–P11, P7–P17, P13–P23 and P19–P5 for the crack case 1 ($N=24$, $r=165 \text{ mm}$). By comparing the first wave packet of these four paths, it could be concluded that the existence of the damage in P1–P11 led to a decrease in its amplitude, because

Fig. 8 a Phase velocity dispersion curve for the aluminum plate, b four-cycle sin tone burst

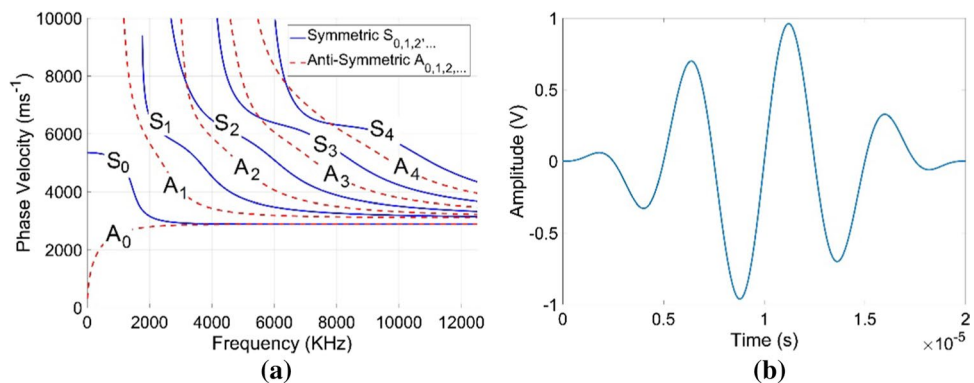


Fig. 9 von Mises stress distribution (Pa) when the 4-cycle tone burst was applied at P2: **a** at 33 μs after excitation; **b** at 48 μs after excitation

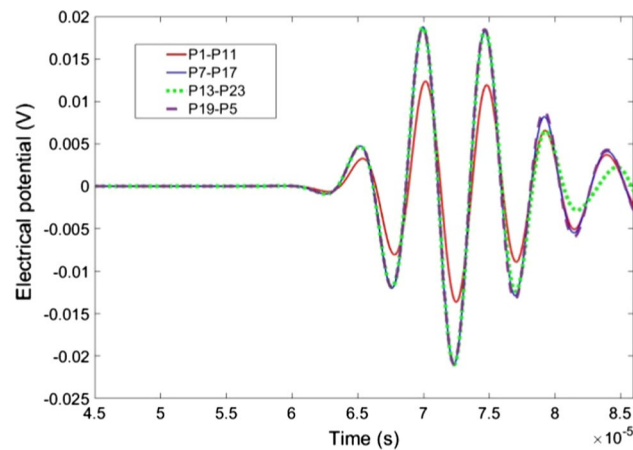
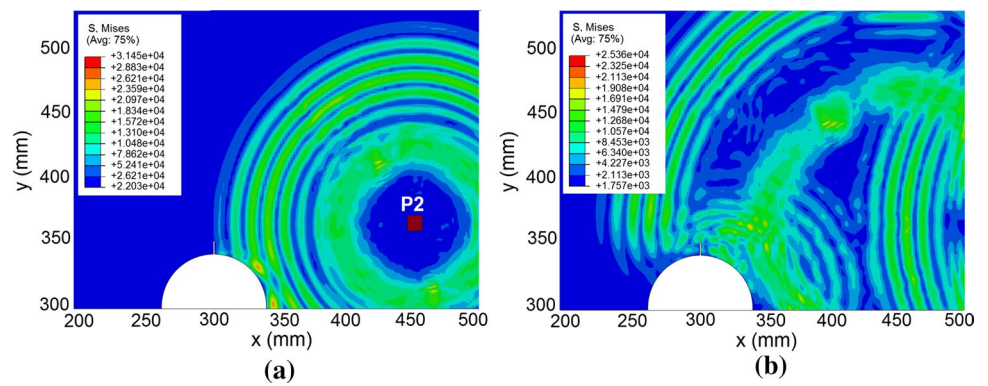


Fig. 10 Signal comparison of undamaged and damaged paths in similar paths

a part of the sent waves was reflected after interacting with the damage.

4 Damage Identification in the Plate with a Hole

The energy of wavelet detail coefficients $D^m(n)$ and wavelet approximate coefficients $A^m(n)$ obtained from DWT in each decomposition level m can be calculated as:

$$E_D^m = \sum_n |D^m(n)|^2 \tag{13}$$

$$E_A^m = \sum_n |A^m(n)|^2 \tag{14}$$

First, wavelet energy of approximate coefficients obtained from DWT of the first wave packet of all similar paths is calculated to detect the damage. This energy is measured for the first four decomposition levels m . Then, the following

four features are measured for calculated coefficients in each P_i-P_j :

$$(F_k)_{i-j} = \prod_{L=1}^k (E_A^L)_{i-j}; \quad k = 1, 2, 3, 4. \tag{15}$$

F_1 is the wavelet energy of approximate coefficients at the first wavelet decomposition level ($m = 1$) computed using Eq. (13). Moreover, F_2 , F_3 , and F_4 are calculated from producing approximate coefficients energy of the first two, first three and four decomposition levels, respectively. When one path in a group of similar paths passes through the damage, the amplitude of the first wave packet and F_k value measured for this path are less than the other paths in the group. The value of $(F_k)_{i-j}$ is determined for all similar paths. Then, the ratio of the relative change (RC) of the feature is obtained for each group and k , using the following equation separately:

$$(RC_k)_{i-j} = \left| \frac{(F_k)_{\max} - (F_k)_{i-j}}{(F_k)_{\max}} \right| \tag{16}$$

where $(F_k)_{\max}$ is the maximum of $(F_k)_{i-j}$ among the sensing paths mentioned in each group. In each group of similar paths, the path with greatest energy is assumed as the reference, and its RC is 0. The other paths in this group of similar paths will be used to compare with reference. The four values of RC were computed for all sensing paths. The RC value obtained for the sensing paths affected by the damage was more than those obtained for other paths. Moreover, when the damage was along the connecting line of the sensor and actuator, the RC value was higher than when it was near the connecting line of the sensor and actuator. In addition, when no damage is found in existing paths in each group, RC obtained for all similar paths is nearly zero. Thus, the proposed method can identify a defect at the hole edge without analyzing the intact structure by comparing the calculated F_k feature for the paths mentioned in each group of similar paths. In each group of similar paths, if at least one path is not affected by the damage, this path is considered as the reference. However, if all the paths considered in each group

are affected by the damage, the path with greatest $(F_k)_{i-j}$ is considered as the reference. In this case, the proposed method may not be able to detect one of the damages at the hole edge. Therefore, it can be said that the approach is baseline free provided that part of the array is not affected by damage. Moreover, when this method is applied to a metal plate structure, the sensor layout is determined by careful investigation of the structure geometry to define similar paths. In fact, the proposed approach does not consider any data taken from the intact plate, neither to detection of damage nor to determine sensor layout. The main objective of this part of the SHM system is to indicate the plate defect without any information about the damage location. This study considered only the first wave packet of signal and ignored other parts.

In order to detect the location of damage, the values of RC are calculated for all paths. Finally, the plate is divided into $1 \text{ mm} \times 1 \text{ mm}$ elements, and the damage index (DI) in each element situated at a location (x, y) is computed as:

$$DI_k(x, y) = \sum_{l=1}^{N_p} (RC_k)_l \cdot W_l[r_l(x, y)] \quad (17)$$

where N_p is the total number of paths, and $(RC_k)_l$ is the relative change associated with the k th feature at the l th sensing path. $W_l[r_l(x, y)]$ is the probabilistic weight for the l th sensing path at (x, y) (Bagheri et al. 2013). Parameter, $r_l(x, y)$, is defined as the relative distance of the node (x, y) from the actuator location (x_a, y_a) and the sensor location (x_s, y_s) associated with the l th sensing path, that is:

$$r_l(x, y) = \frac{\sqrt{(x - x_a)^2 + (y - y_a)^2} + \sqrt{(x - x_s)^2 + (y - y_s)^2}}{\sqrt{(x_a - x_s)^2 + (y_s - y_a)^2}} \quad (18)$$

If the element (x, y) is located on the connecting line between the actuator and the sensor, the value of r is equal to 1, and when there is distance, this value decreases. In this study, the probabilistic weight is considered as (Bagheri et al. 2013)

$$W_l[r_l(x, y)] = \exp \left[- \left(\frac{r_l(x, y)}{\beta} \right)^2 \right] \quad (19)$$

where β is the constant which is between 0 and 1 to control the influence width of travel path across a transducer pair. This parameter is determined by the trial-and-error method depending on the distance between actuator and sensor. A small β reduces affected zone identified by transducer pairs. Therefore, a defect near the travel path across a pair of transducers may be undetectable. Conversely, a large coefficient enlarges affected zone, making perception conservative. In this study, β is considered as 0.002.

4.1 Damage Detection Results

In the following, the performance of the four features introduced in Eq. (15) in identifying the crack location (for $N=24$, and $r=165 \text{ mm}$). In Figs. 11, 12, and 13, the values of DI calculated using the four features are shown for the crack cases 2, 3, and 4, respectively. DI coefficients obtained for all cases of damage were normalized to 1. Also, these figures show the results after applying an arbitrary threshold. In this study, a threshold of 0.7 is considered for the DI to highlight the damage location, allowing a visual comparison with the actual damage of the structure. The crack location is shown with a white line in these figures. Also, the predicted point with maximum DI is shown by a black star. The number of elements in which DI is larger than the threshold is presented in Table 3. For crack case 2 (Fig. 11), the results obtained from the analysis F_1 and F_2 can accurately identify the damage location. Comparing Fig. 11b, d, it can be said that the DI values obtained from the analysis of feature F_2 compared to F_1 identified damage location more accurately because in Fig. 11d, non-zero area around the crack is smaller than other figures. As shown in Fig. 11e–h, DI values obtained from F_3 and F_4 analysis in some undamaged areas are higher than 0.7. Furthermore, the DI results showed that the maximum of the DI obtained from the analysis of F_3 and F_4 is not precisely located in the actual damage (see Fig. 11e, g). Therefore, for crack case 2, the results obtained from analysis of features F_3 and F_4 do not have acceptable performance in identifying the damage location.

For crack case 3 (Fig. 12), DI values obtained from the analysis of F_1 at the upper part of the crack are smaller than 0.7 (see Fig. 12a, b). Thus, the results obtained for feature F_1 (with and without threshold) could not to identify the upper part of the crack. As shown in Fig. 12e, g, results obtained from analysis of features F_3 and F_4 cannot correctly identify the crack location because the DI values are close to one in the undamaged areas around the hole. However, as shown in Fig. 12c, the DI values obtained from the analysis of feature F_2 are close to one only in the areas around the crack. Therefore, for crack case 3, only DI values obtained from the analysis of F_2 could localize the damage. According to Table 3 and comparing the results obtained from analyzing F_2 with those of F_3 and F_4 , it can be concluded that the number of the elements larger than the threshold is less for F_2 , with the nonzero area being smaller.

For crack case 4 (Fig. 13), the results obtained from analyzing all four features introduced in Eq. (15) can accurately identify the damage location. The results of Table 3 and F_1 , F_2 , F_3 , and F_4 analyses show that the number of the elements larger than the threshold is less for F_2 , with the nonzero area being smaller. Thus, the results obtained from analyzing F_2 can identify the damage location more precisely.

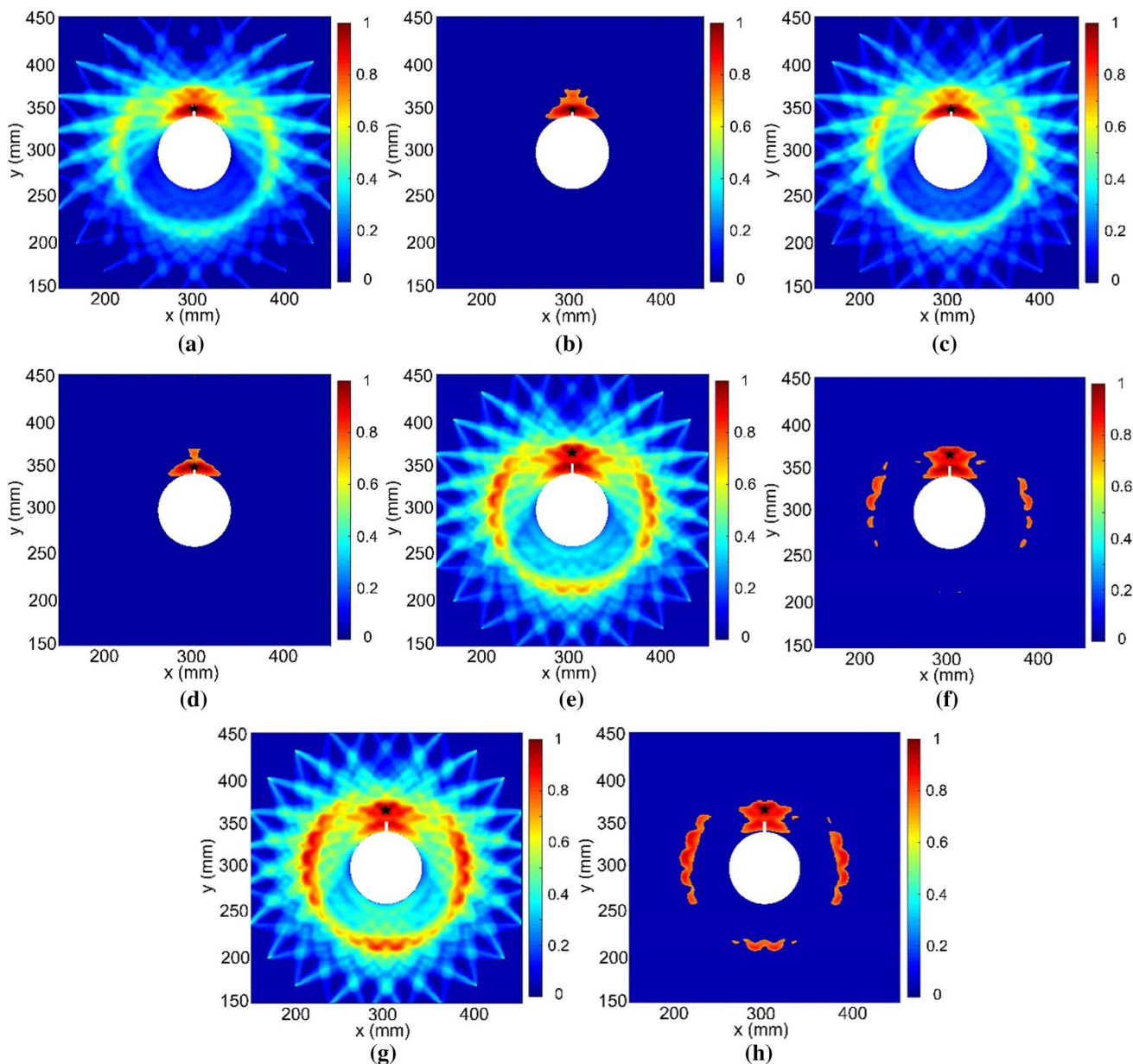


Fig. 11 Damage detection results obtained from analysis of **a** F_1 without threshold, **b** F_1 with threshold, **c** F_2 without threshold, **d** F_2 with threshold, **e** F_3 without threshold, **f** F_3 with threshold, **g** F_4 without threshold, **h** F_4 with threshold (for crack case 2)

By comparing the results obtained from analysis of features F_1 , F_2 , F_3 , and F_4 (Figs. 11, 12, 13), it can be concluded that DI values calculated by using feature F_2 can detect the location of the damage better than other features.

Next, the crack identification capability of the proposed damage index is compared with the damage index technique introduced in Ref. (Stawiarski et al. 2017). In this reference, first, the area between the response signal from the intact ($f_{int}(t)$) and defected ($g_{def}(t)$) structure is calculated to obtain damage index through Eq. 20.

$$NumInt = \int_a^b [f_{int}(t) - g_{def}(t)] dt \tag{20}$$

The increase in area ($NumInt$) indicates a disturbance in the response signal due to the structural defect observed in the wave propagation path between the actuator and the sensor. The damage index DI at each node position (x, y) is defined as follows (Stawiarski et al. 2017):

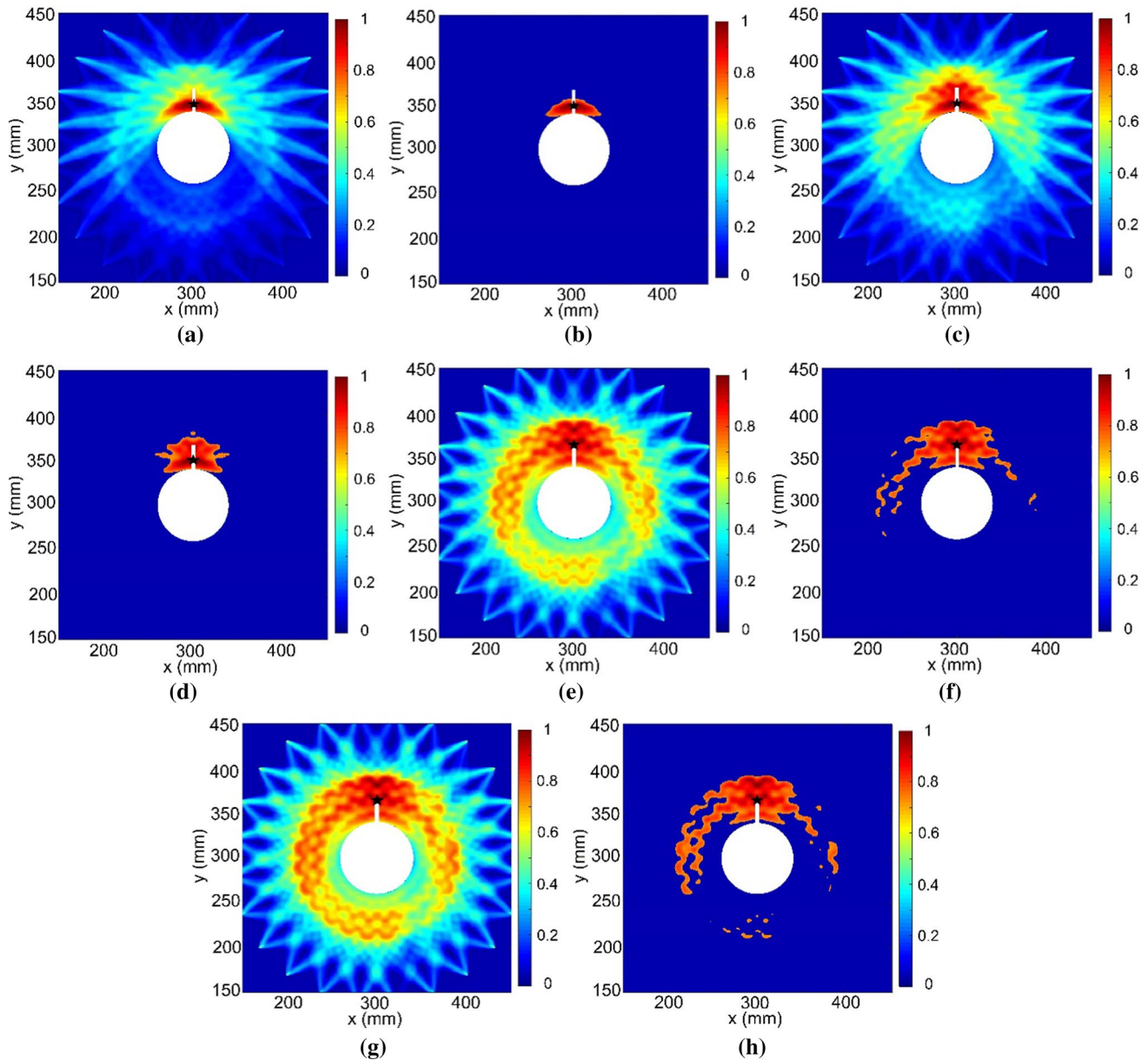


Fig. 12 Damage detection results obtained from analysis of **a** F_1 without threshold, **b** F_1 with threshold, **c** F_2 without threshold, **d** F_2 with threshold, **e** F_3 without threshold, **f** F_3 with threshold, **g** F_4 without threshold, **h** F_4 with threshold (for crack case 3)

$$DI(x, y) = \sum_{k=1}^N \text{NumInt.} \left(\frac{\beta - R(\Omega)}{\beta - 1} \right) \quad (21)$$

$$R(\Omega) = \begin{cases} R_c(\Omega), & R_c(\Omega) < \beta \\ \beta, & R_c(\Omega) \geq \beta \end{cases} \quad (22)$$

$$R_c(\Omega) = \frac{\sqrt{(x - x_{ak})^2 + (y - y_{ak})^2} + \sqrt{(x - x_{sk})^2 + (y - y_{sk})^2}}{\sqrt{(x_{ak} - x_{sk})^2 + (y_{ak} - y_{sk})^2}} \quad (23)$$

$\Omega = [x, y, x_{ak}, y_{ak}, x_{sk}, y_{sk}]$ is a function of the variables connected with the localization of the actuator (x_{ak}, y_{ak}) and sensor (x_{sk}, y_{sk}). The Damage Index is calculated for each wave propagation path between an actuator and each sensor. In Fig. 14, the DI values calculated by Eq. (21) (Stawiarski et al. 2017) are shown for the three crack cases 2–4, when 24 transducers are placed on the circumference of a circle with the radius 165 mm ($N=24, r=165$ mm). This damage index definition can precisely detect the crack location introduced in cases 2 and 4, but the DI values in some undamaged areas are higher than the considered threshold. This method cannot detect the upper part of the radial crack for crack case 3.

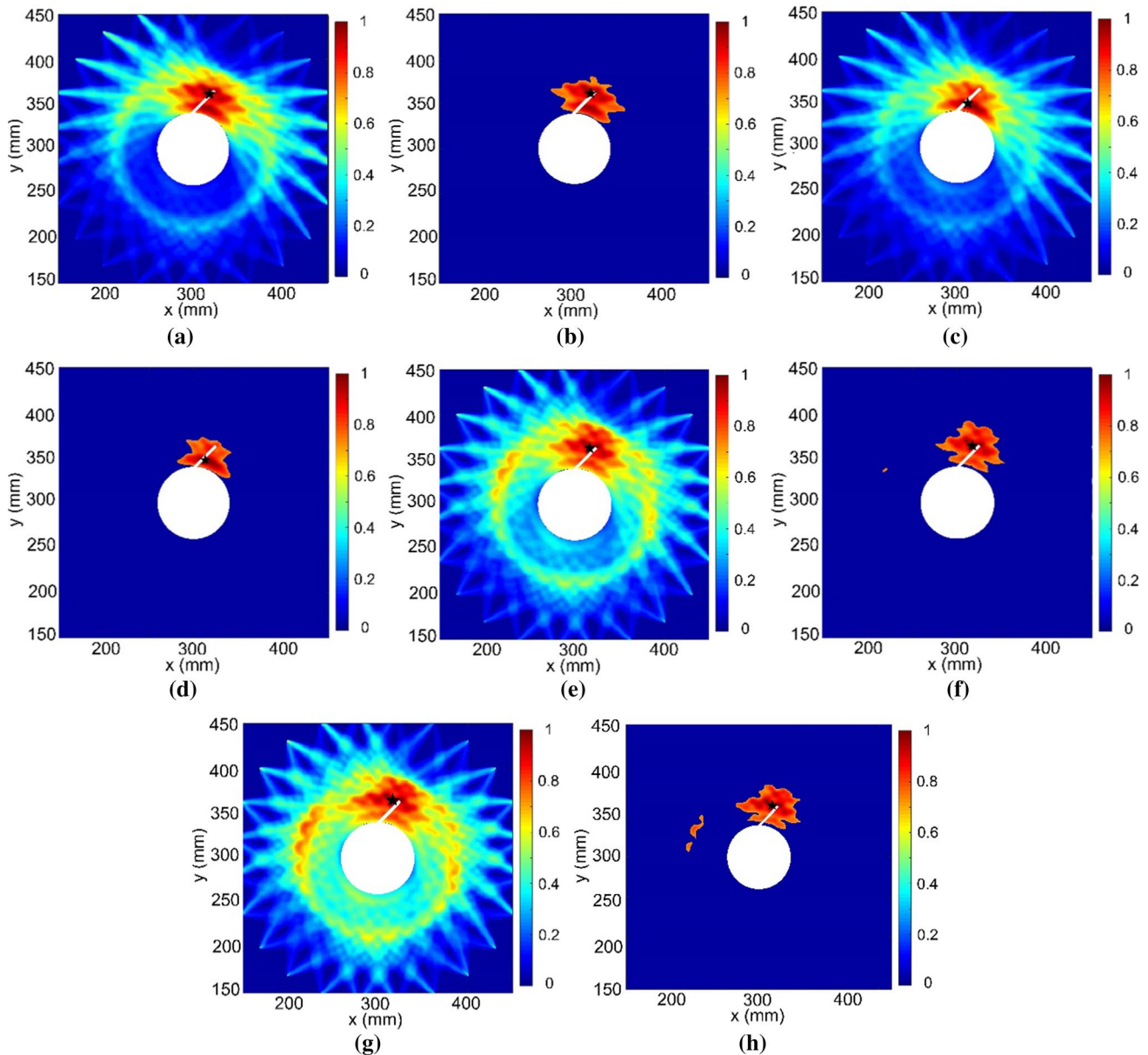


Fig. 13 Damage detection results obtained from analysis of **a** F_1 without threshold, **b** F_1 with threshold, **c** F_2 without threshold, **d** F_2 with threshold, **e** F_3 without threshold, **f** F_3 with threshold, **g** F_4 without threshold, **h** F_4 with threshold (for crack case 4)

The comparison of Fig. 14a–c and Figs. 11d, 12d, and 13d reveal that the DI introduced in Ref. (Stawiarski et al. 2017) has poorer performance than the DI calculated by Eq. (17) in identifying the crack that appeared at the hole edge.

In addition, for the case study 1, the effects of the number and location of transducers in identifying the damage location were examined. For crack cases 1 and 3, the analysis results of the measured signals for 12, 18, and 24 transducers ($N=12, 18, 24$) are shown in Figs. 15, 16 and 17. These transducers are located at distances of 110, 165, and 220 mm from the center of the middle hole ($r=110, 165, 220$ mm). As shown in Fig. 15, when the simulated PZTs are located at

distance of 110 mm from the center of the middle hole, the location of the crack with length of 5 mm and 25 mm can be well identified by considering 18 or 24 PZTs (see Fig. 15b, c, e, f). However, only a part of the crack with length of 25 mm can be detected considering the 12 PZTs. This is because, when 18 or 24 PZTs are at distance of $r=110$ mm, the sight line of the actuator–sensor pair of a group of similar paths passes near the edge of the hole (see Fig. 7b, c, blue lines). Therefore, the proposed method can identify the small cracks on the hole edge by comparing the energy of wavelet coefficients obtained from the DWT of these similar paths. However, for $r=110$ mm and $N=12$, the actuator–sensor

Table 3 Number of elements with DI larger than threshold

Crack case	Feature	Number of elements with DI larger than 0.7
Case 2	F_1	1053
	F_2	821
	F_3	2548
	F_4	3990
Case 3	F_1	798
	F_2	1873
	F_3	4514
	F_4	6213
Case 4	F_1	2212
	F_2	1463
	F_3	2275
	F_4	2683

line of sight of all paths pass with a short distance from the hole edge (see Fig. 7a, blue lines). Therefore, for crack case 1, although the damage has affected in the first wave packet of some similar paths, the proposed method cannot accurately identify the damage location (see Fig. 15a). In addition, the proposed method cannot detect the initial part of the crack on the hole edge for crack case 3 (see Fig. 15d).

As shown in Fig. 16, when the simulated PZTs are located at 165 mm from the center of the middle hole, the proposed method can correctly detect the location of both crack cases by considering 24 PZTs (see Fig. 16c, f). However, the analysis results of the signals measured for 12 PZTs can only detect the crack with length of 5 mm and the initial part of the crack with length of 25 mm. The reason is that the actuator–sensor sight line of a group of similar paths passes near the edge of the hole for $N=12$ and $r=165$ mm (see Fig. 7a, red lines). However, the line of sight of the similar paths considered in the other two groups of similar

paths does not pass through the crack. Therefore, it is necessary to consider more PZTs around the hole to detect all crack parts. As shown in Fig. 16b, e, the results obtained for the 18 PZTs cannot detect the initial part of the crack on the hole edge because the actuator–sensor sight line of all paths passes with a short distance from the hole edge (see Fig. 7b, red lines). For $N=24$ and $r=165$, as shown in Fig. 6a, the actuator–sensor line of sight of the first group of similar paths passes near the edge of the hole. According to Fig. 6b, c, the actuator–sensor connecting line of the other two groups of similar paths passes with a short distance from the hole edge. When one path in a group of similar paths passes through or near the damage, the energy of the first wave packet of this path should be lower than the other paths in this group of similar paths. Thus, for crack case 3, the proposed method can detect all crack parts with a length of 25 mm because the actuator–sensor connection line of some of the paths introduced in the first two groups passes through or near the damage (see Fig. 16f).

For the crack cases 1 and 3, the images of the probability distribution for the defect location are illustrated in Fig. 17 when the 12, 18, and 24 PZTs are placed on the circumference of a circle with a radius of 220 mm. For crack case 1, the analysis results of the signals measured for 18 PZTs accurately detect the location of the damage (see Fig. 18b). However, the results obtained for 12 and 24 PZTs, although they detect the presence of a crack in the upper part of the hole, but do not correctly detect its location (Fig. 18a, c). This is because for 18 PZTs, the actuator–sensor line of sight of a group of similar paths passes near the edge of the hole (see Fig. 7b, path P11–P1), but for 12 and 24 PZTs, this line passes with a short distance from the hole edge (see Fig. 7a, c, black lines). According to the results shown in Fig. 17d–f, for crack case 3, the proposed method can detect only a part of the crack, and more PZTs are needed to detect all parts of the crack.

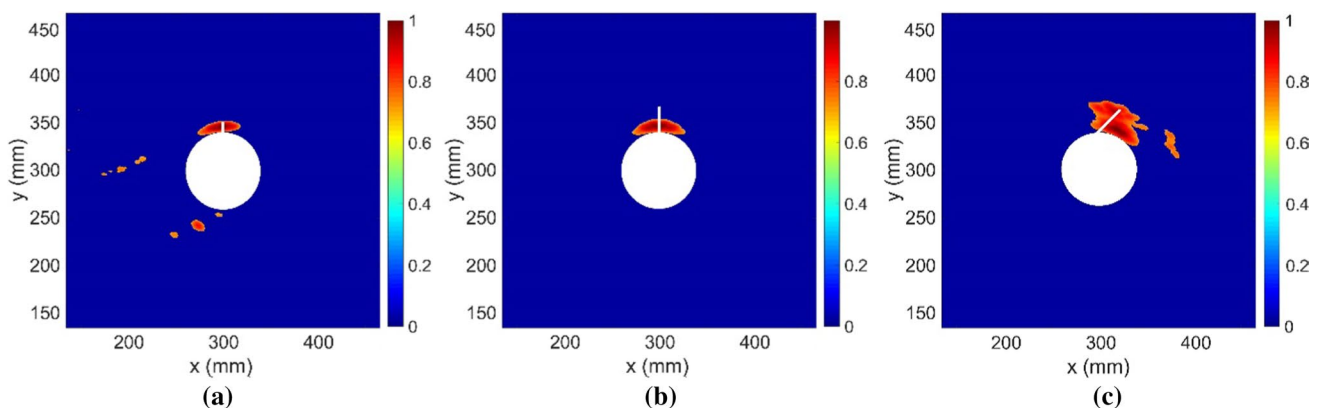


Fig. 14 Damage detection results on the plate-like structure using the DI values calculated by Eq. (19) (Stawiarski et al. 2017) for **a** crack case 2, **b** crack case 3, **c** crack case 4

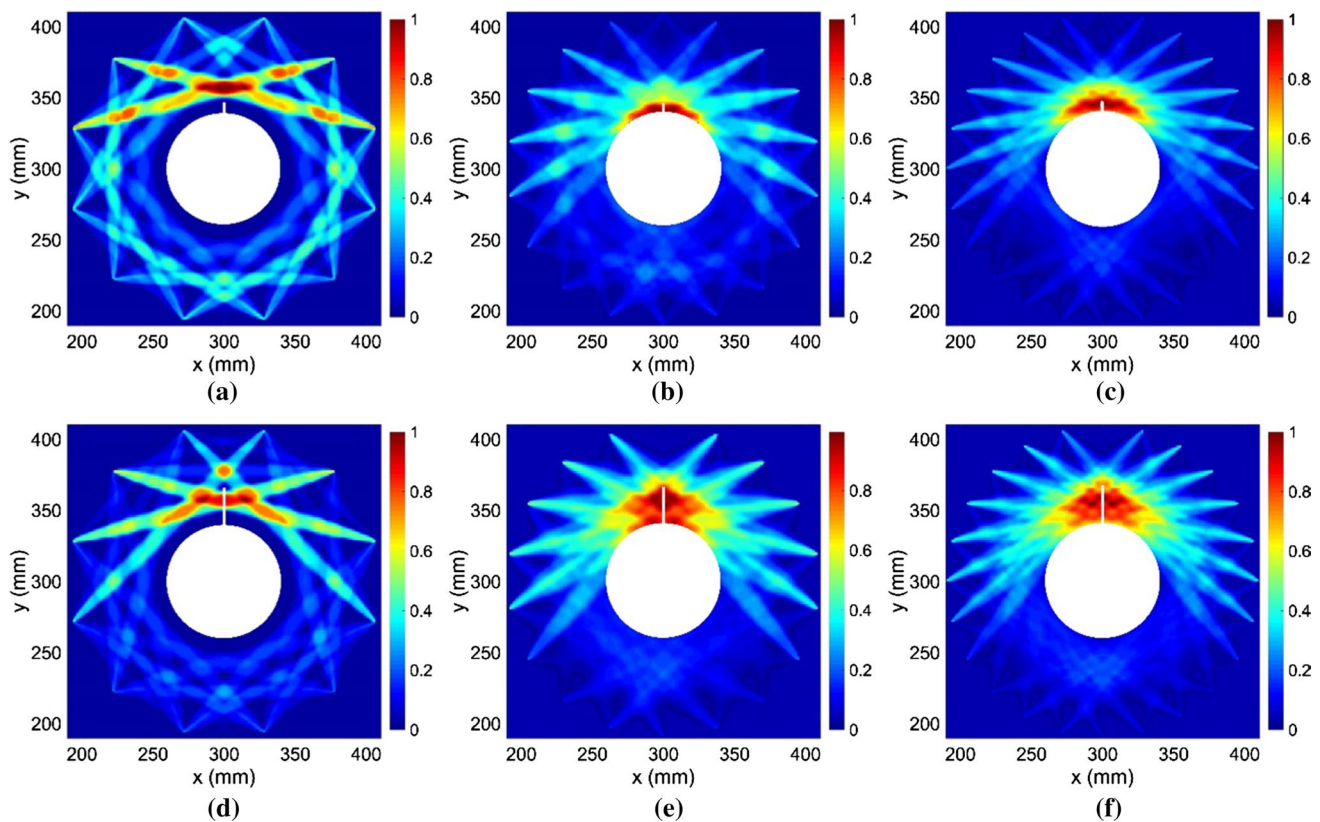


Fig. 15 Damage detection results obtained for the different number of transducers when they are located at distance of 110 mm from the center of hole: **a** for crack case 1, $N=12$, **b** for crack case 1, $N=18$, **c**

for crack case 1, $N=24$, **d** for crack case 3, $N=12$, **e** for crack case 3, $N=18$, **f** for crack case 3, $N=24$

The comparison of Figs. 15, 16 and 17 shows that the sight line of a group of similar paths should pass near the hole edge to detect the initial part of the crack at the edge of the hole. In addition, the proposed method needs a dense sensor array to detect all parts of a crack that occurred at the hole edge. The greater the distance of the transducers from the hole center, the more transducers are needed to detect the damage location. Only the results obtained for ($N=18$, $r=110$ mm), ($N=24$, $r=110$ mm), ($N=24$, $r=165$ mm) can identify the crack with different lengths of 5 mm and 25 mm. Similar conclusions can be drawn for cracks with different lengths of 10 mm, 15 mm, and 20 mm, which are not presented here for the sake of space.

4.2 Effects of Boundary Reflections

The three case studies 2–4 were employed to investigate the effect of the plate boundaries on the damage detection results. In these plates, 18 PZTs with a distance of 110 mm from the hole center were considered to detect crack at the hole edge. In the second case study, the minimum distance between the simulated PZTs to the left edge of the plate was approximately 40 mm, and in the third and fourth case

studies, the minimum distance was approximately 30 mm and 20 mm, respectively. For the three case studies 2, 3, and 4, the damage detection results of crack length 5 mm are illustrated in Fig. 18a–c, respectively. The results shown in Figs. 18a and 15b are similar. Therefore, it can be concluded that in the case of study 2, the waves reflected from the plate edges did not affect the damage detection results. Also, as shown in Fig. 18b, c, the results obtained for the third and fourth case studies cannot correctly identify the crack location. This is because, the wave reflected from the plate edge affected the first wave packet due to the proximity of some PZTs to the left side edge of the plate. Therefore, the transducers located around the hole should be at least 40 mm away from the plate sides to avoid wave reflection effects, which is easy to implement for sensor layout.

4.3 The Capability to Identify Multi-damage

In the following two examples, the performance of the recommended method was investigated to determine multiple cracks appearing at the hole edge. For this purpose, in the first case study, two damage states at the edge of the central hole are considered. In each damage state, two

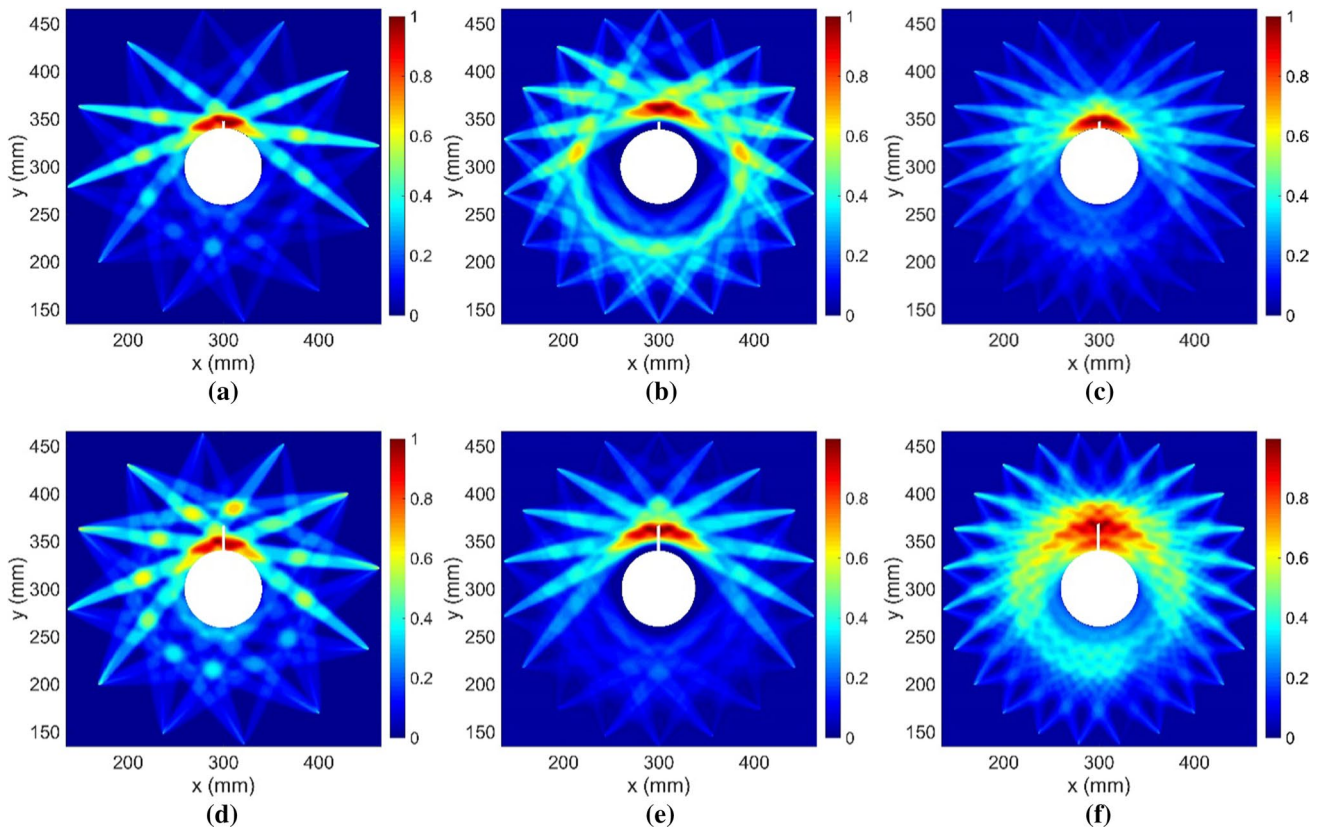


Fig. 16 Damage detection results obtained for the different number of transducers when they are located at distance of 165 mm from the center of hole: **a** for crack case 1, $N=12$, **b** for crack case 1, $N=18$, **c**

for crack case 1, $N=24$, **d** for crack case 3, $N=12$, **e** for crack case 3, $N=18$, **f** for crack case 3, $N=24$

through-thickness radial cracks with different lengths and orientations measured clockwise from the y -axis are considered. In Fig. 19, the location of the cracks is illustrated schematically in the damaged plate. For the first and second damage states, the map of the plate in terms of the DI computed using Eq. (17) is shown in Fig. 20a, b, respectively, when 24 transducers are placed on the circumference of a circle with the radius 165 mm. The results obtained from the F_2 analysis are shown in this figure. In Fig. 20a, b, the values of DI obtained at the location of both cracks are larger than other locations. Furthermore, in Fig. 20a, the area around the 0° orientation crack is darker than the 135° orientation crack, indicating more severe damage.

4.4 Effect of Noise

In reality, the signals recorded by the sensors have noise all the times. For simulation purposes the numerical data is polluted with noise using the procedure applied in (Bagheri et al. 2013, 2017; Tang et al. 2019) in which the presented methods were also verified numerically. To test the robustness of the proposed method under the influence of noise, Zero-mean and unit-variance Gaussian white noise was

added to the simulation results of output signals for all paths using the MATLAB command *awgn*. This command is a signal function, the signal-to-noise ratio (SNR), and the power of the signal. It should be noted that smaller SNR values correspond to larger noise levels. For crack case 1 ($N=24$, $r=165$ mm), the proposed algorithm was then applied using noise contaminated signals with four SNR levels equal to 9 dB, 7 dB, 5 dB, and 3 dB, respectively. For this damaged plate, the DI values computed using the F_2 feature corrupted with different noise levels are presented in Fig. 21. The comparison of Figs. 21a–d and 16c show some differences that are not significant. Similar conclusions can be drawn for the other crack cases that are not presented here due to space limitation. Thus, the presented approach is robust against some random noise in ultrasonic signals and exhibits strong resistance to the influence of a large level of noise influence.

4.5 Damage Identification in the Plate with an Elliptic Hole

In this section, the performance of the proposed method to identify cracks at the elliptical hole edge is investigated. We consider a 600 mm \times 600 mm \times 1.59 mm cantilever

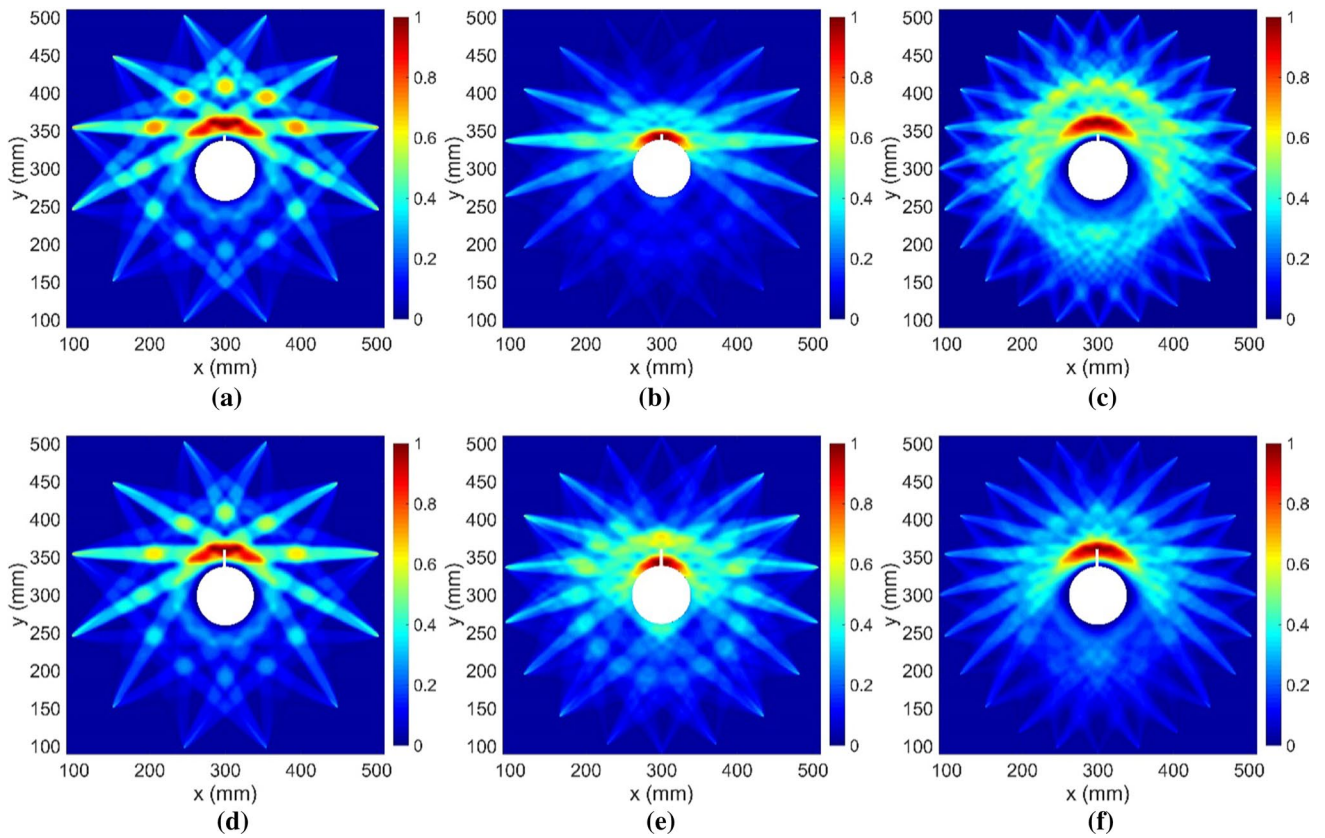


Fig. 17 Damage detection results obtained for the different number of transducers when they are located at distance of 220 mm from the center of hole: **a** for crack case 1, $N=12$, **b** for crack case 1, $N=18$, **c** for crack case 1, $N=24$, **d** for crack case 3, $N=12$, **e** for crack case 3, $N=18$, **f** for crack case 3, $N=24$

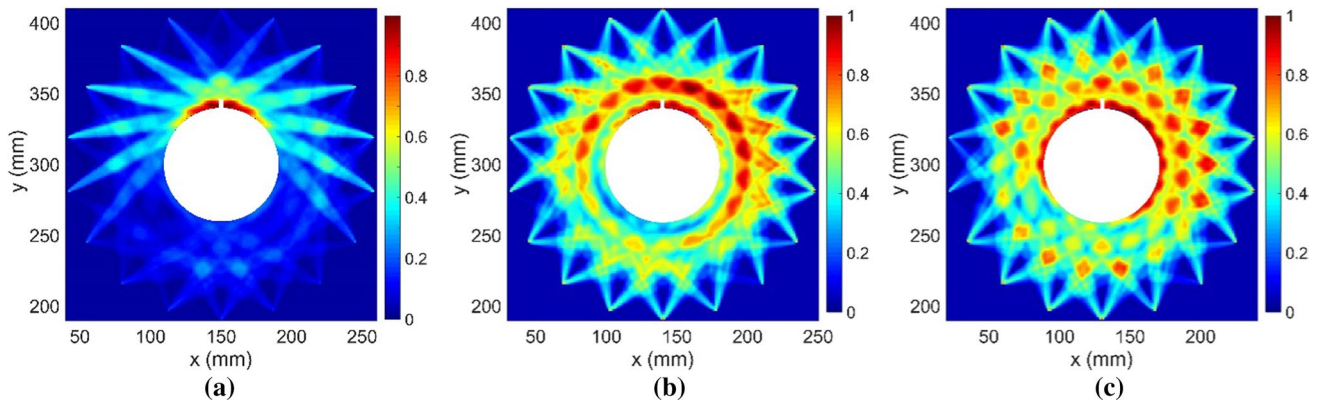


Fig. 18 Images of the probability distribution for the location of the crack with length of 5 mm: **a** case study 2, **b** case study 3, **c** case study 4

aluminum plate (Al-6061) containing a central elliptical hole. The dimensions of the hole in the x and y directions were 120 mm and 80 mm, respectively. In this plate, a crack was considered with dimensions 3 mm × 1 mm × 1.59 mm at the edge of the hole. Figure 22a shows the plate geometry and damage location at the elliptical hole edge. In order to

identify small cracks created at the hole edge and detect the passing path of the first wave packet (shortest distance between actuator and sensor), the transducers should be placed around the middle hole so that the straight line of the actuator–sensor passes near the edge of the hole. A total of 24 circular piezoelectric transducers were placed on the

Fig. 19 Geometry of an aluminum square plate with two cracks at the hole edge: **a** damage state 1, **b** damage state 2

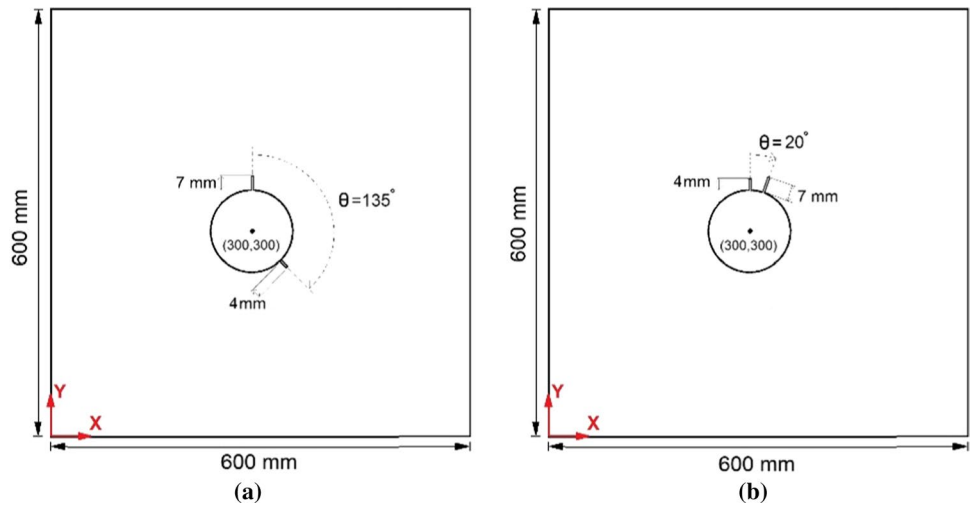
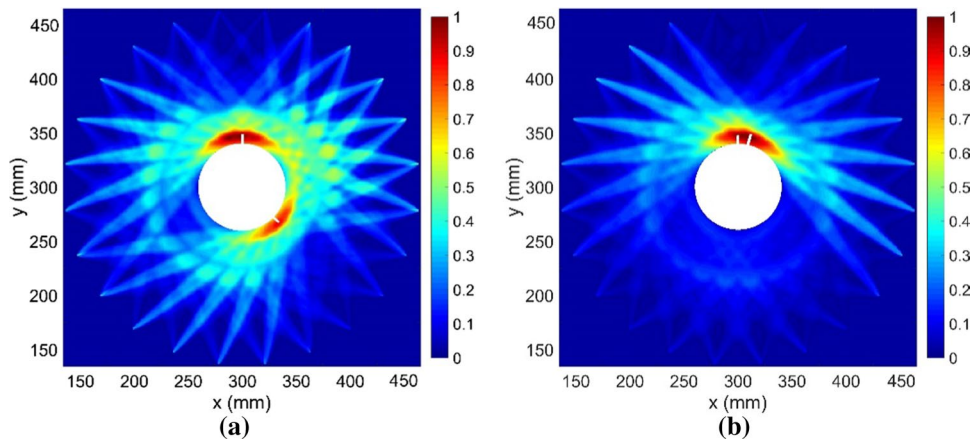


Fig. 20 Damage detection results on the aluminum plate with two cracks at the hole edge: **a** damage state 1, **b** damage state 2



circumference of an ellipse with dimensions 300 mm and 450 mm in the x and y directions, respectively, to detect the defect in this plate (see Fig. 22a). The 4-cycle tone burst was applied on 24 simulated PZT actuators ($P_i, i = 1, 2, \dots, 24$), respectively. Meanwhile, the signals of the three PZTs mentioned in following relation were measured.

$$\begin{cases} \text{for } i = 1, 2, \dots, 6 & \Rightarrow P_{i+14}, P_{i+15}, P_{i+16} \\ \text{for } i = 7, 8, \dots, 12 & \Rightarrow P_{i+8}, P_{i+9}, P_{i+10} \\ \text{for } i = 13, 14, \dots, 18 & \Rightarrow P_{i-8}, P_{i-9}, P_{i-10} \\ \text{for } i = 19, 20, \dots, 24 & \Rightarrow P_{i-14}, P_{i-15}, P_{i-16} \end{cases} \quad (24)$$

There are $24 \times 3 = 72$ received signals in total. Since aluminum is isotropic, sufficient conditions of a similar path need the equal PZT spacing of transmitter–receiver paths and the same position to the edges of the hole. Thus, all paths are separated as 18 groups of similar paths, as shown in Table 4. Figure 22b shows schematically all the sensing paths mentioned in groups 1–6 of Table 4. Since the actuator–sensor sight line of these paths passes near the hole edge,

so by analyzing them, a small crack created at the hole edge can be identified. Generally, the configuration of the transducers and the grouping of similar paths should change by altering the hole geometry.

For the damaged plate shown in Fig. 22a, the value of the damage index calculated using Eq. (17) based on the F_2 feature is illustrated in Fig. 23. As shown in this figure, the DI values obtained around the crack are higher than in other areas. Therefore, it can be said that the proposed method can detect the location of the crack with acceptable accuracy.

5 The Effects of Uncertainty in the Length of Similar Paths

As described before, this study proposed a baseline free defect identification method based on similar paths. The sensor spacing of transmitter–receiver paths had to be equal in these similar paths. Here, the effects of uncertainty in the

Fig. 21 Damage detection results obtained from analysis of F_2 feature for crack case 1 with different noise levels in ultrasonic signals: **a** SNR = 9 dB, **b** SNR = 7 dB, **c** SNR = 5 dB, **d** SNR = 3 dB

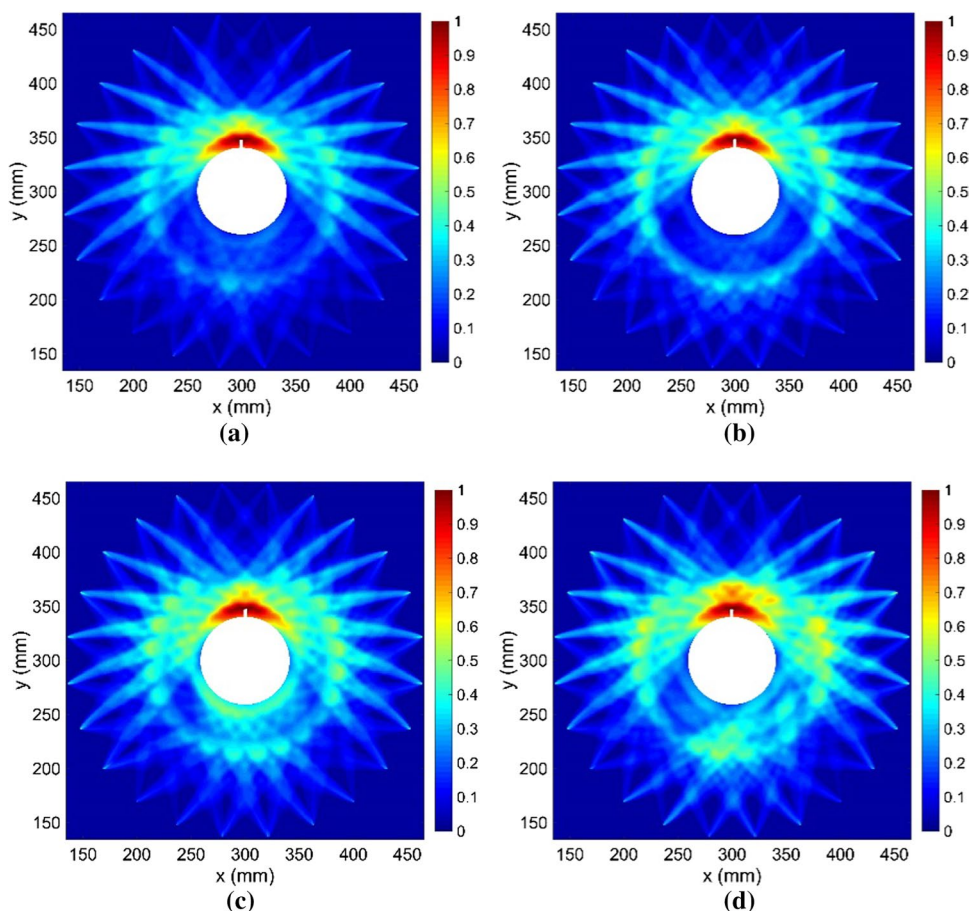
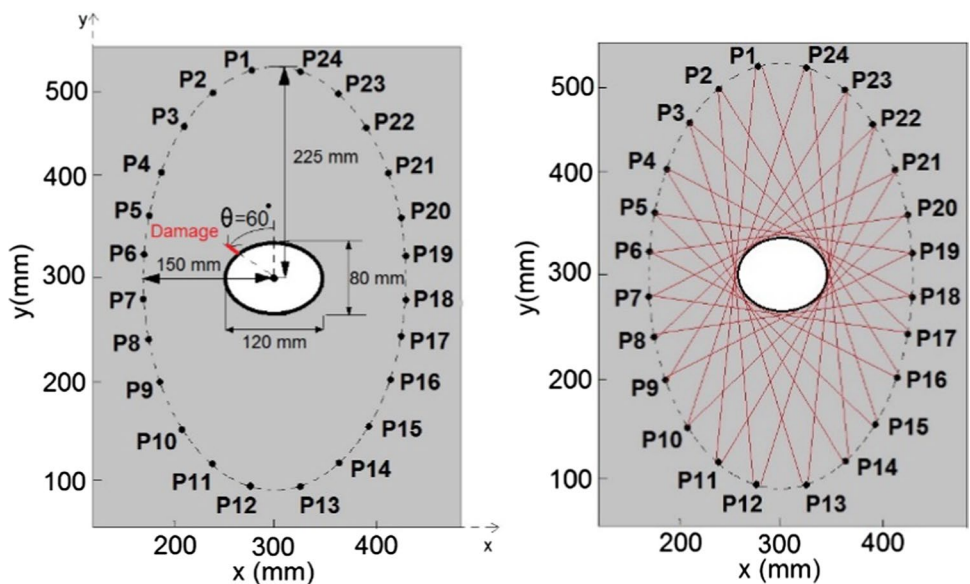


Fig. 22 a Schema of the multi-point measuring system in the plate with an elliptic hole; **b** the sensing paths mentioned in groups 1–6



length of similar paths which could be due to the inaccuracy in the installation of sensors on plate, on the accuracy of damage detection results are investigated. To this purpose,

for the first case study ($N = 24, r = 165 \text{ mm}$), the DI values obtained for various amounts of dislocations of transducer P1 along the x-direction in the absence of any damage are

Table 4 Grouping all of the sensing paths for elliptical PZT pattern

Group no	Similar paths	Group no	Similar paths
1	P1–P15, P12–P22, P13–P3, P24–P10	10	P4–P19, P9–P18, P16–P7, P21–P6
2	P2–P16, P11–P21, P14–P4, P23–P9	11	P5–P20, P8–P17, P17–P8, P20–P5
3	P3–P17, P10–P20, P15–P5, P22–P8	12	P6–P21, P7–P16, P18–P9, P19–P4
4	P4–P18, P9–P19, P16–P6, P21–P7	13	P1–P17, P12–P20, P13–P5, P24–P8
5	P5–P19, P8–P18, P17–P7, P20–P6	14	P2–P18, P11–P19, P14–P6, P23–P7
6	P6–P20, P7–P17, P18–P8, P19–P5	15	P3–P19, P10–P18, P15–P7, P22–P6
7	P1–P16, P12–P21, P13–P4, P24–P9	16	P4–P20, P9–P17, P16–P8, P21–P5
8	P2–P17, P11–P20, P14–P5, P23–P8	17	P5–P21, P8–P16, P17–P9, P20–P4
9	P3–P18, P10–P19, P15–P6, P22–P7	18	P6–P22, P7–P15, P18–P10, P19–P3

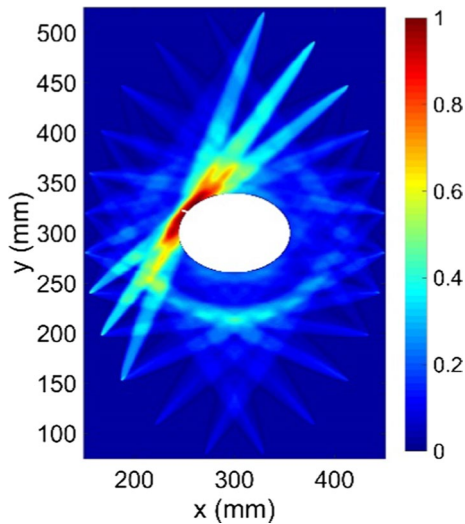


Fig. 23 Damage detection results for the damaged plate with an elliptic hole using the DI values calculated by Eq. (17)

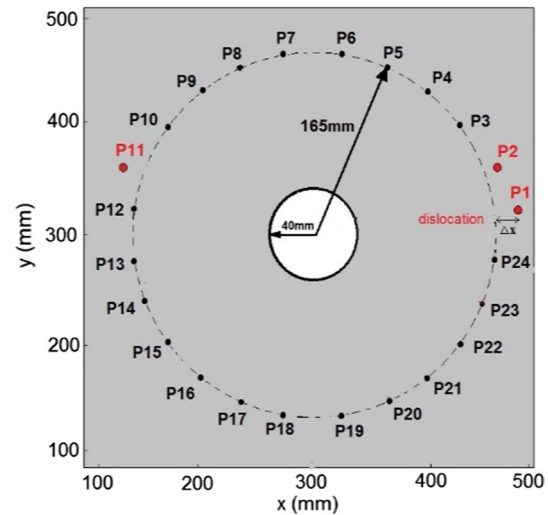


Fig. 24 Dislocation of P1, P2 and P11 transducers

Table 5 DI values for various dislocations of transducer P1

Transducer dislocation (mm)	DI (for the sensing path P1–P11)
0.25	0.0031
0.5	0.0038
0.75	0.0052
1	0.0071
1.5	0.01
2	0.0132
3	0.017

shown in Table 5 (see Fig. 24). According to the results shown in this table, for a range of dislocations between 0.25 and 3 mm, the maximum value of DI obtained for the sensing path P1–P11 is 0.017. It is clear that as the amount

Table 6 DI values of sensing path P1–P11 obtained for various crack size

Crack size (mm)	DI (for the sensing path P1–P11)
3	0.403
5	0.504
10	0.612
15	0.701
20	0.812

of dislocation increases, the calculated DI value increases. Because no damage is considered at the edge of the hole, and given that all transducers are at the same distance from the edge of the hole, the results shown in Table 5 can be considered for the dislocation of other transducers. Also, Table 6 presents the DI values defined by Eq. (17) for the sensing path P1–P11 versus the crack size. The location of crack is shown in Fig. 4a. As shown in Fig. 6a, the actuator–sensor

line of sight of this path passes through the crack. According to the results shown in Table 5, for a small crack with the length of 3 mm, the value of DI is 0.403, which is more than 20 times the DI value calculated for 3 mm dislocation of transducer P1. Therefore, comparing the results shown in Tables 4 and 5, it can be concluded that the effect of crack in the value of DI is much greater than the effect of transducer dislocation.

In the next example, the effect of transducer dislocation on the measured F_2 for healthy and damaged paths is investigated. For crack cases 2 and 3, the numerical results of damage detection are investigated for a range of dislocations between 0.5 and 2 mm. First, P1, P2 and P11 piezoelectrics are shifted by 0.5, 1, and 2 mm in x-direction (see Fig. 15). Then, the effects of these dislocations on F_2 values obtained for paths P1–P9, P1–10, P1–11, P2–P10, P2–P11, P2–P12, P11–P19, P11–P20 and P11–P21 are investigated. It should

be noted that the actuator–sensor line of sight of any of paths P11–P19, P11–P20, P11–P21, P1–P11, and P2–P12 does not pass through the damage, while the actuator–sensor line of sight of paths P1–P9 and P2–P10 passes through the damage. Also, for crack case 2, the actuator–sensor line of sight of paths P1–P10 and P2–P11 does not pass through the damage, while for crack case 3, the actuator–sensor line of sight of these paths passes through the damage. Therefore, the effects of dislocation on the damaged and undamaged paths are investigated. The results are presented in Table 7. Due to the results of this table, when the deviation of transducers locations from their desired positions is less than 2 mm, maximum error created in F_2 values is 3.8%. Therefore, the proposed damage detection method is not sensitive to dislocation of transducers which can occur through installation process.

Table 7 F_2 values for various dislocation of P1, P2 and P11 transducers

Sensing path	Dislocation of transducer (mm)	Crack case 2		Crack case 3	
		F_2 value $\times 10^{-7}$	Error (%)	F_2 value $\times 10^{-8}$	Error (%)
P1–P9	0.5	2434.6	0.5	11,767	0.8
	1	2430.9	0.7	11,746	1
	2	2415	1.2	11,670	1.6
P1–P10	0.5	627.7	0.4	845.5*	1.9
	1	623.75	1	840.4*	2.5
	2	621.13	1.4	839.8*	2.6
P1–P11	0.5	34.29*	1.5	46.03*	2.6
	1	33.96*	2.4	45.85*	3
	2	33.68*	3.2	45.57*	3.53
P2–P10	0.5	2794.8	0.5	8443	0.8
	1	2781.3	0.9	8409.1	1.3
	2	2758	1.8	8326.5	2.2
P2–P11	0.5	627.15	0.8	728.9*	1.6
	1	624.85	1.1	723.4*	2.4
	2	616.43	2.5	722.2*	2.6
P2–P12	0.5	33.65*	2.4	43.72*	2
	1	33.47*	2.9	43.21*	3.2
	2	33.43*	3	42.93*	3.8
P11–P19	0.5	2554.3	0.3	25,543	0.3
	1	2551.8	0.4	25,518	0.4
	2	2541.6	0.8	25,416	0.8
P11–P20	0.5	694.72	0.4	6947.2	0.4
	1	692.65	0.7	6926.5	0.7
	2	689.91	1.1	6899.1	1.1
P11–P21	0.5	87.02	0.4	870.2	0.4
	1	86.76	0.7	867.6	0.7
	2	86.25	1.3	862.5	1.3

*Damaged path

6 Conclusion

In this article, the wave propagation method was used to design the SHM system for the identification of the crack localized near the hole in the plate-like structures. This study proposed a baseline free defect identification method based on similar paths. The proposed method did not need any data taken from a pristine plate and could detect the damage location only by comparing the energy of the coefficients wavelet calculated for similar paths. This method relies on the fact that the measured signals of two similar paths will be identical if no damage is present in the vicinity of the paths. Note that the proposed SHM scheme was baseline free, provided that the material is isotropic, that is, the attenuation and the dispersion are not dependent on the direction of propagation, and the sensitivity of the probing devices is very similar. The proposed damage detection algorithm was validated numerically using a commercial finite element software. The results showed that this method could detect the location of the multiple cracks that occurred at the hole edge only through the wavelet energy of approximate coefficients at the first and second levels of the wavelet decomposition. In addition, the proposed method could detect cracks in the edge of the hole with different geometries. It should be noted that the configuration of the transducers and the grouping of similar paths depended on the hole geometry. In order to identify small cracks created at the hole edge, the transducers should be placed around the hole so that the actuator–sensor straight line of a group of similar paths passes near the edge of the hole. Moreover, the transducers located around the hole should be at least 4 cm away from the plate sides to avoid wave reflection effects, which is easy to implement for sensor layout. The proposed baseline free method required a dense sensor array to determine crack location accurately. When there is a hole in the plate and crack length at hole edge is large, many sensors are needed to define similar paths which identify entire cracked area. However, it is challenging to determine the entire cracked area by a few sensors. It is a common problem for most of guided wave-based SHM methods. To test the robustness of the proposed method under the influence of noise, the recorded time waveforms were corrupted with different noise levels, and the maps of the plate with and without added noise were compared. The results showed that the DI based on a probabilistic approach could localize the crack regardless of noise. Moreover, the influence of uncertainties in the length of sensing paths, which can occur on the plate in the sensors installation process, were investigated on the accuracy of damage detection results. The results showed that the sensitivity of the feature extracted from DWT to the dislocation of transducers is

low and negligible. The results are promising and future studies should focus on the experimental validation of the methodology.

References

- Addison PS (2002) The illustrated wavelet transform handbook: introductory theory and applications in science, engineering, medicine and finance. CRC Press, Boca Raton
- Alem B, Abedian A, Nasrollahi-Nasab K (2016) Reference-free damage identification in plate-like structures using Lamb-wave propagation with embedded piezoelectric sensors. *J Aerosp Eng* 29(6):04016062. [https://doi.org/10.1061/\(ASCE\)AS.1943-5525.0000646](https://doi.org/10.1061/(ASCE)AS.1943-5525.0000646)
- Alleyne DN, Pavlakovic B, Lowe MJS, Cawley P (2004) Rapid, long range inspection of chemical plant pipework using guided waves. *Key Eng Mater* 270:434–441. <https://doi.org/10.4028/www.scientific.net/KEM.270-273.434>
- Bagheri A, Li K, Rizzo P (2013) Reference-free damage detection by means of wavelet transform and empirical mode decomposition applied to Lamb waves. *J Intell Mater Syst Struct* 24(2):194–208. <https://doi.org/10.1177/1045389X12460433>
- Bagheri A, Rizzo P, Li K (2017) Ultrasonic imaging algorithm for the health monitoring of pipes. *J Civ Struct Health Monit* 7(1):99–121. <https://doi.org/10.1007/s13349-017-0214-y>
- Barski M, Stawiarski A (2018) The crack detection and evaluation by elastic wave propagation in open hole structures for aerospace application. *Aerosp Sci Technol* 81:141–156. <https://doi.org/10.1016/j.ast.2018.07.045>
- Bartoli I, di Scalea FL, Fateh M, Viola E (2005) Modeling guided wave propagation with application to the long-range defect detection in railroad tracks. *NDT E Int* 38(5):325–334. <https://doi.org/10.1016/j.ndteint.2004.10.008>
- Bourasseau N, Moulin E, Delebarre C, Bonniau P (2000) Radome health monitoring with Lamb waves: experimental approach. *NDT E Int* 33(6):393–400. [https://doi.org/10.1016/S0963-8695\(00\)00007-4](https://doi.org/10.1016/S0963-8695(00)00007-4)
- Cawley P (2018) Structural health monitoring: closing the gap between research and industrial deployment. *Struct Health Monit* 17(5):1225–1244. <https://doi.org/10.1177/1475921717750047>
- Chiu WK, Rose LRF, Vien BS (2017) Scattering of the edge-guided wave by an edge crack at a circular hole in an isotropic plate. *Procedia Eng* 188:309–316. <https://doi.org/10.1016/j.proeng.2017.04.489>
- Courant R, Friedrichs K, Lewy H (1967) On the partial difference equations of mathematical physics. *IBM J Res Dev* 11(2):215–234. <https://doi.org/10.1147/rd.112.0215>
- Dai W, Wang X, Zhang M, Zhang W, Wang R (2019) Corrosion monitoring method of porous aluminum alloy plate hole edges based on piezoelectric sensors. *Sensors* 19(5):1106. <https://doi.org/10.3390/s19051106>
- Ebrahimkhanlou A, Salamone S (2018) Single-sensor acoustic emission source localization in plate-like structures using deep learning. *Aerospace* 5(2):50. <https://doi.org/10.3390/aerospace5020050>
- Faccioli E, Maggio F, Paolucci R, Quarteroni A (1997) 2D and 3D elastic wave propagation by a pseudo-spectral domain decomposition method. *J Seismol* 1(3):237–251. <https://doi.org/10.1023/A:1009758820546>
- Ghadami A, Behzad M, Mirdamadi HR (2018) Damage identification in multi-step waveguides using Lamb waves and scattering

- coefficients. *Arch Appl Mech* 88(6):1009–1026. <https://doi.org/10.1007/s00419-018-1355-0>
- Giridhara G, Rathod VT, Naik S, Mahapatra DR, Gopalakrishnan S (2010) Rapid localization of damage using a circular sensor array and Lamb wave based triangulation. *Mech Syst Signal Process* 24(8):2929–2946. <https://doi.org/10.1016/j.ymsp.2010.06.002>
- Gómez Muñoz CQ, García Márquez FP, Hernández Crespo B, Makaya K (2019) Structural health monitoring for delamination detection and location in wind turbine blades employing guided waves. *Wind Energy* 22(5):698–711. <https://doi.org/10.1002/we.2316>
- Grabowska J, Palacz M, Krawczuk M (2008) Damage identification by wavelet analysis. *Mech Syst Signal Process* 22(7):1623–1635. <https://doi.org/10.1016/j.ymsp.2008.01.003>
- Gresil M, Giurgiutiu V, Shen Y, Poddar B (2012) Guidelines for using the finite element method for modeling guided lamb wave propagation in SHM processes. In: 6th European workshop on structural health monitoring, pp 3–6
- He J, Ran Y, Liu B, Yang J, Guan X (2017) A fatigue crack size evaluation method based on lamb wave simulation and limited experimental data. *Sensors* 17(9):2097. <https://doi.org/10.3390/s17092097>
- Hua J, Cao X, Yi Y, Lin J (2020) Time–frequency damage index of Broadband Lamb wave for corrosion inspection. *J Sound Vib* 464:114985. <https://doi.org/10.1016/j.jsv.2019.114985>
- Ihn JB, Chang FK (2008) Pitch-catch active sensing methods in structural health monitoring for aircraft structures. *Struct Health Monit* 7(1):5–19. <https://doi.org/10.1177/1475921707081979>
- Jingpin J, Xiangji M, Cunfu H, Bin W (2017) Nonlinear Lamb wave-mixing technique for micro-crack detection in plates. *NDT E Int* 85:63–71. <https://doi.org/10.1016/j.ndteint.2016.10.006>
- Kim J, Zhu B, Cho Y (2019) An experimental study on second harmonic generation of guided wave in fatigued spring rod. *J Mech Sci Technol* 33(9):4105–4109. <https://doi.org/10.1007/s12206-019-0805-0>
- Kumar Y, Dewal ML, Anand RS (2012) Relative wavelet energy and wavelet entropy based epileptic brain signals classification. *Biomed Eng Lett* 2(3):147–157. <https://doi.org/10.1007/s13534-012-0066-7>
- Lanza Discalea F, Matt H, Bartoli I, Coccia S, Park G, Farrar C (2007) Health monitoring of UAV wing skin-to-spar joints using guided waves and macro fiber composite transducers. *J Intell Mater Syst Struct* 18(4):373–388. <https://doi.org/10.1177/1045389X06066528>
- Lee BC, Staszewski WJ (2007) Lamb wave propagation modelling for damage detection: II. Damage monitoring strategy. *Smart Mater Struct* 16(2):260. <https://doi.org/10.1088/0964-1726/16/2/004>
- Legendre S, Massicotte D, Goyette J, Bose TK (2000) Wavelet-transform-based method of analysis for Lamb-wave ultrasonic NDE signals. *IEEE Trans Instrum Meas* 49(3):524–530. <https://doi.org/10.1109/19.850388>
- Liu S, Du C, Mou J, Martua L, Zhang J, Lewis FL (2013) Diagnosis of structural cracks using wavelet transform and neural networks. *NDT E Int* 54:9–18. <https://doi.org/10.1016/j.ndteint.2012.11.004>
- Liu S, Liu F, Yang Y, Li L, Li Z (2020) Nondestructive evaluation 4.0: ultrasonic intelligent nondestructive testing and evaluation for composites. *Res Nondestruct Eval* 31(5–6):370–388. <https://doi.org/10.1080/09349847.2020.1826613>
- Mallat SG (1989) A theory for multiresolution signal decomposition: the wavelet representation. *IEEE Trans Pattern Anal Mach Intell* 11(7):674–693. <https://doi.org/10.1109/34.192463>
- Masurkar FA, Yelve NP (2017) Lamb wave based experimental and finite element simulation studies for damage detection in an aluminium and a composite plate using geodesic algorithm. *Int J Acoust Vib* 22(4):413–421. <https://doi.org/10.20855/ijav.2017.22.4486>
- Moser F, Jacobs LJ, Qu J (1999) Modeling elastic wave propagation in waveguides with the finite element method. *NDT E Int* 32(4):225–234. [https://doi.org/10.1016/S0963-8695\(98\)00045-0](https://doi.org/10.1016/S0963-8695(98)00045-0)
- Ng CT, Veidt M (2009) A Lamb-wave-based technique for damage detection in composite laminates. *Smart Mater Struct* 18(7):074006. <https://doi.org/10.1088/0964-1726/18/7/074006>
- Rizzo P, di Scalea FL (2006) Feature extraction for defect detection in strands by guided ultrasonic waves. *Struct Health Monit* 5(3):297–308. <https://doi.org/10.1177/1475921706067742>
- Rubio JJ, Kashiwa T et al (2019) Multi-class structural damage segmentation using fully convolutional networks. *Comput Ind* 112:103121. <https://doi.org/10.1016/j.compind.2019.08.002>
- Schubert Kabban C, Uber R, Lin K, Lin B, Bhuiyan MY, Giurgiutiu V (2018) Uncertainty evaluation in the design of structural health monitoring systems for damage detection. *Aerospace* 5(2):45. <https://doi.org/10.3390/aerospace5020045>
- Sohn H, Park HW, Law KH, Farrar CR (2007) Damage detection in composite plates by using an enhanced time reversal method. *J Aerosp Eng* 20(3):141–151. [https://doi.org/10.1061/\(ASCE\)0893-1321\(2007\)20:3\(141\)](https://doi.org/10.1061/(ASCE)0893-1321(2007)20:3(141))
- Stark HG (2005) Wavelets and signal processing: an application-based introduction. Springer, Berlin
- Stawiarski A, Barski M, Pająk P (2017) Fatigue crack detection and identification by the elastic wave propagation method. *Mech Syst Signal Process* 89:119–130. <https://doi.org/10.1016/j.ymsp.2016.08.023>
- Tang Z, Munir N, Lee TG, Yeom YT, Song SJ (2019) Lamb wave flaw classification in Al plates using time reversal and deep neural networks. *J Korean Phys Soc* 75(12):978–984. <https://doi.org/10.3938/jkps.75.978>
- Wan X, Zhang Q, Xu G, Tse PW (2014) Numerical simulation of nonlinear lamb waves used in a thin plate for detecting buried micro-cracks. *Sensors* 14(5):8528–8546. <https://doi.org/10.3390/s140508528>
- Wang D, Ye L, Lu Y (2009) A probabilistic diagnostic algorithm for identification of multiple notches using digital damage fingerprints (DDFs). *J Intell Mater Syst Struct* 20(12):1439–1450. <https://doi.org/10.1177/1045389X09338323>
- Wang Y, Guan R, Lu Y (2017) Nonlinear Lamb waves for fatigue damage identification in FRP-reinforced steel plates. *Ultrasonics* 80:87–95. <https://doi.org/10.1016/j.ultras.2017.05.004>
- Wang T (2014) Finite element modelling and simulation of guided wave propagation in steel structural members. Doctoral dissertation, University of Western Sydney, Australia
- Xu ZD, Zhu C, Shao LW (2021) Damage identification of pipeline based on ultrasonic guided wave and wavelet denoising. *J Pipeline Syst Eng Pract* 12(4):04021051. [https://doi.org/10.1061/\(ASCE\)PS.1949-1204.0000600](https://doi.org/10.1061/(ASCE)PS.1949-1204.0000600)
- Yu Y, Ou J, Li H (2010) Design, calibration and application of wireless sensors for structural global and local monitoring of civil infrastructures. *Smart Struct Syst* 6(5_6):641–659. https://doi.org/10.12989/SSS.2010.6.5_6.641
- Zhou L, Sun H, He Z (2013) Fractal dimension-based damage imaging for composites. *Shock Vib* 20(5):979–988. <https://doi.org/10.3233/SAV-130798>